ORIGINAL ARTICLE



Post-Capture Tethered-Debris Principal Moment of Inertia Estimation via Pinhole Camera Model with Occlusion

Derek Bourabah¹ · Chris Gnam¹ · Eleonora M. Botta¹

Accepted: 21 August 2024
© The Author(s), under exclusive licence to American Astronautical Society 2024

Abstract

The post-capture control of tethered debris can be challenging due to its unresponsive and uncooperative nature. Often, control of debris may require knowledge of the moments of inertia, which are usually unknown. This study applies an Unscented Kalman Filter to estimate the attitude, angular rates, and principal moments of inertia of debris captured via a tether. The filter utilizes tension and pixel-coordinate measurements of various landmarks on the debris to achieve estimation. Due to the translational and rotational motion of the debris, landmarks can be occluded or exit the field of view of the camera. Different control profiles are applied to the chaser to investigate the effects of the tension in the tether and of the visibility of chosen landmarks. It is found that large tension in the tether does not provide more accurate estimates, but that prolonging transient tether behavior improves the accuracy and precision of moment of inertia estimates. It is further observed that lower tension magnitudes with longer visibility times of landmarks make estimation of the inertia parameters possible with fewer tracked landmarks.

Keywords Parameter estimation · Moments of inertia · Unscented Kalman Filter · Space debris · Tethered debris · Pinhole camera model

Derek Bourabah derekbou@buffalo.edu

Chris Gnam crgnam@buffalo.edu

Published online: 18 September 2024

Department of Mechanical and Aerospace Engineering, University at Buffalo, 240 Bell Hall, Buffalo, NY 14260-4400, USA



Eleonora M. Botta ebotta@buffalo.edu

1 Introduction

40

The importance of removing various large debris in Low-Earth Orbit(LEO) has become apparent due to a rise in on-orbit collisions in recent years [1, 2]. The consequences of inaction can be catastrophic but may be avoided by removing large debris from LEO [3-6]. Numerous debris-removal methods have been proposed, with some promising strategies involving tethered capture. Tethered capture may be performed through tethered nets [7–11], harpoons [12–14], or tethered robots [15–18], and is often safer than the conventional robotic arm method of capture. Tethers provide a flexible connection between the chaser and debris which allows for larger capture distances, but increases target control difficulty. Moreover, control of the target is critical as winding of the tether around the target, or improper control applied through the tether, may lead to loss of control of the chaser or even a collision between the chaser and target [19]. Difficulties with post-capture control are caused by the unresponsive and uncooperative nature of debris, the properties and states of which are also largely unknown. Post-capture control difficulties are exacerbated by the possibility of the onset of chaos due to the coupled dynamics of the chaser and debris [20-22].

Numerous control strategies have been applied to solve the post-capture attitude control problem [23-29]; however, controls can often be improved by, or even require, the moments of inertia of the target and other state information. In the case of tethered robotic capture, Huang et al. created an adaptive controller to account for the estimation of the moments of inertia properties and for unknown torques on the target [16]. Estimation of the moments of inertia is often performed after robotic capture of debris, as the moments affecting the debris are often easy to determine through the rigid connection between the chaser and target [30-35]. However, when the affecting moments are unknown, such as during the pre-capture phase, only the ratios of the moments of inertia parameters may be found [36-40]. Work on estimating the inertia tensor after tethered capture of debris is scarce. Zhang et al. estimated one principal mass moment of inertia (MMI) and the difference between two principal moments of inertia using a leastsquares estimator [41]. Huang et al. estimated the inertia tensor after tetheredrobotic capture of debris using a least-squares method and measurements from a gyroscope attached via the robot on the debris [15]. Bourabah et al. estimated the principal moments of inertia of a tethered target using an Extended Kalman Filter and an Unscented Kalman Filter (UKF) using gyro measurements and perfect knowledge of tension in the tether [42]. Later, Bourabah et al. progressed their work by replacing gyro measurements with a camera and tension measurements, while assuming numerous points may be tracked as long as they are within the camera field of view (FOV) [43].

This work improves upon previous work from the authors by including an occlusion model, in which visibility of points may be lost depending on debris orientation, and the effects of J2 acceleration on each spacecraft. An Unscented Quaternion Estimator(USQUE) and UKF are combined to estimate the attitude, angular velocity, and principal moments of inertia of a tether-captured debris



target. Moreover, observability of all debris states with tension measurements and image-processing measurements alone is proved in this work for the first time through the Gramian observability matrix. Assuming that measurements from a camera model with occlusion and from a tension sensor are provided to the filter, new results are obtained: estimation performance is examined with 4 sets of landmarks at different locations of the debris, different control profiles, and different initial conditions. The control profiles and initial conditions are selected to generate (1) rapid rotation of the debris, (2) small rotational motion with little tension variation, and (3) small rotational motion with large tension variation. These different conditions are analyzed to determine preferred debris motion and measurement combination for accurate estimation of the principal moments of inertia. It is found that minor rotational motion with longer periods of tension variation is preferred for estimation performance. Moreover, it is demonstrated that in each case the provided measurements are sufficient to estimate all states of the debris, even when some landmarks are occluded from view. Finally, no significant degradation is found in estimation results where the measurement covariance matrix and the noise covariance have mismatched characteristics.

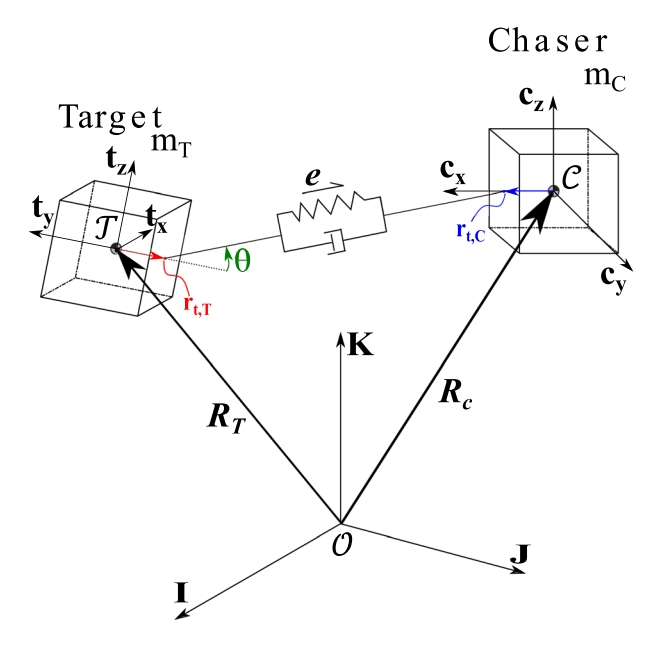
The rest of this paper is organized as follows. The model and dynamics of the chaser-tether-debris system are detailed in Sect. 2. Section 3 provides physical foundations for estimation, which guide the choice of sensors, and presents the camera model and the overall measurement model. The implementation of the UKF and the simulation for data generation are discussed in Sects. 4 and 5, respectively. Section 6 analyzes the performance of the filter with three different control profiles, varying sets of landmarks, and different noise/uncertainty levels; the capabilities of the filter are first discussed, followed by factors that affect estimation. The paper then ends with final conclusions of the work in Sect. 7.

2 System Dynamics

The tethered chaser–debris system consists of a rigid body chaser spacecraft connected to a rigid body debris by a tether as shown in Fig. 1, where the tether is modeled as a single spring-damper element that is unable to withstand compression. The chaser spacecraft is equipped with a camera and a tension sensor in-line with the tether. In Fig. 1, the Earth-Centered Inertial(ECI) reference frame is represented with \mathcal{O} , the chaser frame with \mathcal{C} , and the target body-fixed frame with \mathcal{T} . The direction of the tether is denoted by the unit vector $\underline{\boldsymbol{e}}$. The inertial positions of the chaser craft and the debris body are denoted with $\underline{\boldsymbol{R}}_C$ and $\underline{\boldsymbol{R}}_T$, respectively. The positions of the tether attachment point on the chaser and target relative to their centers of mass are denoted as $\underline{\boldsymbol{r}}_{t,C}$ and $\underline{\boldsymbol{r}}_{t,T}$, respectively. Angle θ is the alignment angle defined as the angle from the body-fixed negative y-axis of the debris to the tether.

The translational dynamics for the chaser and target in the inertial frame are given by:





The Journal of the Astronautical Sciences

Fig. 1 System model with reference frames

$$m\underline{\ddot{R}} = m\left(\underline{a}_p - \mu \frac{\underline{R}}{|\underline{R}||^3}\right) + \underline{T} + \underline{F}$$
 (1)

where μ is the gravitational parameter of earth, m is the mass of the respective spacecraft, T is the tension force applied by the tether on the body, and F are any control forces on the bodies. The only control force in this work is the thrust force on the chaser spacecraft, which will be discussed in Sect. 5. In this work, only the perturbing acceleration due to J2 is considered, which may be calculated as [44]:

$$\underline{\boldsymbol{a}}_{p} = \frac{3J_{2}\mu R_{\text{Earth}}^{2}}{2||\underline{\boldsymbol{R}}||^{5}} \begin{bmatrix} \left(\frac{5R_{K}^{2}}{||\underline{\boldsymbol{R}}||^{2}} - 1\right)R_{I} \\ \left(\frac{5R_{K}^{2}}{||\underline{\boldsymbol{R}}||^{2}} - 1\right)R_{J} \\ \left(\frac{5R_{K}^{2}}{||\underline{\boldsymbol{R}}||^{2}} - 3\right)R_{K} \end{bmatrix}$$
(2)

with the radius of the Earth denoted by R_{Earth} , J_2 denoting the J2 perturbation coefficient, and R_I , R_I , and R_K , being the components of the inertial position of the center of mass of the respective spacecraft.

The attitude motion for the chaser and target is provided by Eq. (3), with all components described in their respective body-fixed frames except for the tension force T, which is described in the inertial frame:



$$\underline{\dot{q}} = \frac{1}{2} \begin{bmatrix} I_{3\times 3} q_4 + S(\underline{q}_{\nu}) \\ -\underline{q}_{\nu}^T \end{bmatrix} \underline{\omega}$$
 (3a)

$$\underline{\dot{\boldsymbol{\omega}}} = \boldsymbol{J}^{-1} \left(\underline{\boldsymbol{\tau}} + \underline{\boldsymbol{r}}_{t} \times (^{\mathcal{X}} \boldsymbol{A}^{\mathcal{O}} \underline{\boldsymbol{T}}) - \underline{\boldsymbol{\omega}} \times \boldsymbol{J} \underline{\boldsymbol{\omega}} \right)$$
 (3b)

where I is the identity matrix, and q is the attitude quaternion of the designated body. The quaternions follow the Shuster notation, in which $\underline{q} = [\underline{q}_{\nu}, q_4]^T$, where $\mathbf{q}_{_{\parallel}} = [q_1,q_2,q_3]^T$ is the vector component and q_4 is the scalar component. The operator S(.) is used to denote a skew-symmetric matrix. Vector \mathbf{r}_{t} is used to represent the tether attachment point on the designated body, and the resultant of the external moments (with the exception of the moment caused by the tension in the tether) is represented with τ . For this work, the only external moments present in this system are the control inputs on the chaser. The tension vector is denoted by Tin the ECI frame and is converted to the body-fixed frame of the respective body using a rotation matrix (i.e., ${}^{\mathcal{X}}A^{\mathcal{O}}$); where \mathcal{X} represents the respective (chaser's or target's) body-fixed frame. When taut, the magnitude of the tension force is calculated as $T = \max(k(l - l_0) + c\dot{l}, 0)$, where the natural length of the tether is given by l_0 , l is the length of the tether at any given time, and \dot{l} is the relative speed of the tether attachment points on the two bodies in the direction of e. The formulation for \dot{l} may be found in prior work by the authors [42]. Parameters k and c are the stiffness and damping coefficients of the tether, respectively. Because of the direction defined for e, the tension force affecting the target is defined as T = Te, whereas the tension affecting the chaser is defined as T = -Te.

3 Measurement Model

Euler's second law for the target, expressed in Eq. (3b), can be simplified as:

$$J\underline{\dot{\omega}} + \underline{\omega} \times (J\underline{\omega}) = \underline{M} \tag{4}$$

where \underline{M} represents the overall external moment applied to the body. Under the assumption that the principal axes of the target are known, the mass matrix of inertia can be written as $J = \text{diag}([J_x, J_y, J_z]^T)$, where J_x , J_y , and J_z denote the principal mass moments of inertia, and $\underline{M} = [M_x, M_y, M_z]^T$. Then, Eq. (4) may be written component-wise as:

$$J_x \dot{\omega}_x + (J_z - J_y) \omega_y \omega_z = M_x \tag{5a}$$

¹ Other external moments (e.g., gravity gradient torque) have been ignored in this work since the moment caused by tension in the tether is significantly greater than perturbative forces, as demonstrated in [43].

$$J_y \dot{\omega}_y + (J_x - J_z) \omega_x \omega_z = M_y \tag{5b}$$

$$J_z \dot{\omega}_z + (J_v - J_x) \omega_x \omega_v = M_z \tag{5c}$$

In this work, the principal mass moments of inertia are unknown and must be determined. The set of three scalar equations in Eq. (5) has a unique solution for the three unknowns if all the angular rates and angular accelerations of the target, as well as the components of the overall moment affecting the target, are known. This calls for measurements of quantities that can provide such information (i.e., coordinates of points on the target in time, and tension force applied on the target).

The necessary measurements are obtained from a tension sensor and camera attached to the chaser spacecraft. While the tension sensor can directly provide noisy measurements of the tension in the tether, a camera would provide pixel coordinates of points in the 3D space. As such, a pinhole camera model is implemented to convert 3D positions to pixel coordinate measurements. The camera frame S is assumed to be at the center of mass of the chaser spacecraft and can be seen in Fig. 2, together with two tracked landmarks (i.e., L_1 and L_2) on the debris.

The pinhole camera projection model used for pixel coordinate measurements of each landmark, γ , is:

$$\underline{\underline{\gamma}} = \begin{bmatrix} d_{x'} \\ d_{y'} \end{bmatrix} = \begin{bmatrix} c_{x'} - s_{x'} \left(\frac{\epsilon_1}{\epsilon_3}\right) \\ c_{y'} + s_{y'} \left(\frac{\epsilon_2}{\epsilon_3}\right) \end{bmatrix}$$
(6)

where the x'- and y'-coordinates of the center of the image in the camera frame are provided by $c_{x'}$ and $c_{y'}$, pixel coordinates of a landmark in the image are represented by $d_{x'}$ and $d_{y'}$, and $s_{x'}$ and $s_{y'}$ are the scales between the image space and the world space, which can be obtained by dividing the image resolution by the sensor size. Vector ϵ is given by:

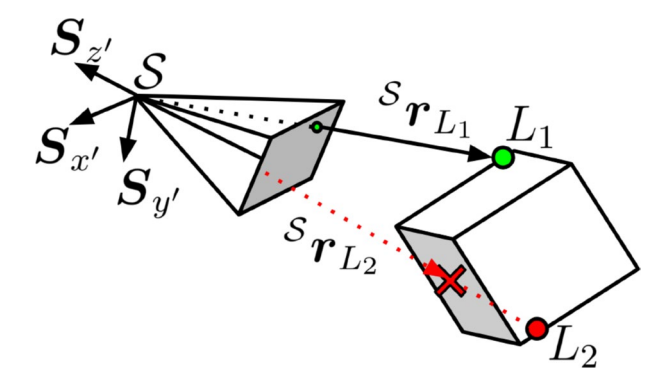


Fig. 2 Camera measurement model geometry



$$\underline{\boldsymbol{\epsilon}} = \begin{bmatrix} \boldsymbol{\epsilon}_1 \\ \boldsymbol{\epsilon}_2 \\ \boldsymbol{\epsilon}_3 \end{bmatrix} = \begin{bmatrix} f & 0 & 0 \\ 0 & f & 0 \\ 0 & 0 & 1 \end{bmatrix} {}^{\mathcal{S}}\underline{\boldsymbol{r}}_L \tag{7}$$

where the focal length of the camera is given by f and ${}^{S}\underline{r}_{L}$ is the position of landmark L in the camera frame S. The position of a landmark relative to the camera in the camera frame may be obtained as:

$${}^{\mathcal{S}}\underline{\boldsymbol{r}}_{L} = ({}^{\mathcal{S}}\boldsymbol{A}^{\mathcal{C}})({}^{\mathcal{C}}\boldsymbol{A}^{\mathcal{O}})\left(({}^{\mathcal{O}}\boldsymbol{A}^{\mathcal{T}})^{\mathcal{T}}\underline{\boldsymbol{r}}_{L} + \underline{\boldsymbol{R}}_{T} - \underline{\boldsymbol{R}}_{C}\right)$$
(8)

where ${}^{T}\underline{r}_{L}$ is the position of a landmark on the debris body in the debris body-fixed frame (assumed to be known in this work).

The pinhole projection model does not take into account the shape model of the target object and will convert any 3D position into the camera frame. However, points that are blocked by the debris body cannot be observed and are said to be "occluded." For example, in Fig. 2, visibility of L_2 is blocked by other parts of the debris' body, and thus the landmark is not visible to the camera. Occlusion is considered in this study and is detailed in Sect. 5.4.

Measurements of both the tension in the tether \tilde{T} and of the pixel coordinates of all tracked landmarks \tilde{y} may then be generated by following:

$$\begin{bmatrix} \tilde{T} \\ \tilde{y} \end{bmatrix} = \underline{h}(\underline{x}) + \underline{v} \tag{9}$$

where the overall measurement model $\underline{\boldsymbol{h}}$ is composed of the tension and pinhole camera models assembled as a vector (i.e., $\underline{\boldsymbol{h}} = [T, \underline{\boldsymbol{\gamma}}_1^T, \dots, \underline{\boldsymbol{\gamma}}_N^T]^T$ for N tracked landmarks), and \boldsymbol{v} is a gaussian white noise vector.

4 Unscented Kalman Filtering

To estimate the angular rates and mass moments of inertia of tethered debris, a standard UKF is employed. The UKF is chosen due to the nonlinear dynamics of the system and its successful application to numerous projects, including previous work on this topic [42]. However, since quaternions are required to satisfy unity constraints, an USQUE [45, 46] is implemented to estimate the attitude (quaternion) of the target debris. The USQUE avoids the need to constrain the UKF quaternion states to obey the unity constraint.

4.1 State Definition

A set of sigma points $\underline{\chi}_k$, selected in a deterministic manner that characterizes a Gaussian distribution, are generated and utilized by the UKF for estimation at each time step. The sigma points are composed of three sets of three parameters, according to $\underline{\chi}_k(i) = [\underline{\delta p}_k^T(i), \underline{\sigma}_k^T(i), \underline{J}_k^T(i)]^T$. This definition represents the estimated



states of the filter: three attitude error angles $\delta p = [\delta p_x, \delta p_y, \delta p_z]^T$ (as described by the USQUE), three angular rates describing the rotation of the body frame with respect to the inertial frame and expressed in the target body frame $\boldsymbol{\omega} = [\omega_{r}, \omega_{v}, \omega_{z}]^{T}$, and three principal moments of inertia parameters $\overline{J} = [J_x, J_y, J_z]^T$ for the target debris. The generated sigma points at the k-th iteration are given by:

The Journal of the Astronautical Sciences

$$\underline{\boldsymbol{\chi}}_{k}(0) = \underline{\boldsymbol{\mu}}_{k} = [\hat{\boldsymbol{\delta p}}_{k}^{T}, \hat{\underline{\boldsymbol{\jmath}}}_{k}^{T}, \hat{\underline{\boldsymbol{J}}}_{k}^{T}]^{T}$$
(10a)

$$\underline{\chi}_{k}(i) = \underline{\sigma}_{k}(i) + \underline{\mu}_{k} \tag{10b}$$

where i denotes a particular sigma point in the set. The states estimated at the k-th iteration are used as the mean of the distribution μ_{L} as per Eq. (10a), while the columns of matrix $\sigma_k = \pm \sqrt{(n+\lambda)P_k}$ are used to create the distribution of sigma points as per Eq. (10b). This gives a total of 2n + 1 sigma points, where n is the number of estimated states (i.e., n = 9 in this problem). The state covariance matrix, P_k , has dimensions of $n \times n$, and λ is a scaling parameter, given by $\lambda = \alpha^2(n + \kappa) - n$, where α and κ are tuning parameters that control the spread of the sigma point distribution and fine-tune higher order moments, respectively. The matrix square root is found using Cholesky decomposition.

4.2 Prediction

Attitude error angles $\underline{\hat{Sp}}_k$ need to be converted to quaternion representations $\underline{\hat{q}}_k(i)$. After an initial estimate of the target's quaternion attitude representation, $\underline{\hat{q}}_0$, is provided to the filter, this conversion can be achieved using:

$$\hat{\underline{q}}_{\iota}(i) = \hat{\delta q}_{\iota}(i) \otimes \hat{q}_{\iota}(0) \tag{11}$$

where $\hat{q}_{_L}(0)$ is the k-th mean attitude quaternion estimate, and the corresponding error quaternion, $\delta q_{L}(i)$, is given by:

$$\underline{\hat{\delta q}}_{k}(i) = \begin{bmatrix} \hat{\delta \varrho}_{k}(i) \\ \hat{\delta q}_{4_{k}}(i) \end{bmatrix} = \begin{bmatrix} (a + \hat{\delta q}_{4_{k}}(i)) \underline{\hat{\delta p}}_{k}(i) / \phi \\ \frac{-a \|\hat{\underline{\delta p}}_{k}(i)\|^{2} + \phi \sqrt{\phi^{2} + (1 - a^{2}) \|\hat{\underline{\delta p}}_{k}(i)\|^{2}}}{\phi^{2} + \|\hat{\underline{\delta p}}_{k}(i)\|^{2}} \end{bmatrix}$$
(12)

where a is a number between 0 and 1 (selected to be 1 in this work) and ϕ is calculated as $\phi = 2(a+1)$. The modified χ_{L} points in the UKF are now given as $\underline{\chi}_{k,m}(i) = [\hat{\underline{q}}_k^T(i), \hat{\underline{\underline{o}}}_k^T(i), \hat{\underline{\underline{f}}}_k^T(i)]^T$. A 4th-order Runge-Kutta integrator is then used to obtain the predicted sigma points by propagating each of the modified sigma points through the system dynamics:



$$\underline{\dot{x}}_{m} = \begin{bmatrix} \dot{\hat{q}}_{1} \\ \dot{\hat{q}}_{2} \\ \dot{\hat{q}}_{3} \\ \dot{\hat{q}}_{4} \\ \dot{\hat{\omega}}_{x} \\ \dot{\hat{\omega}}_{y} \\ \dot{\hat{c}}_{z} \\ \dot{\hat{f}}_{x} \\ \dot{\hat{f}}_{y} \\ \dot{\hat{f}}_{z} \\ \dot{\hat{f}}_{z}$$

where r_x , r_y , and r_z are the components of the tether attachment point position in the body-fixed frame of debris, ${}^T\underline{r}_{t,T}$. The propagation dynamics uses the estimated components of the tension force in the debris body-fixed frame since they depend on the estimated attitude of the debris and the measured tension magnitude \tilde{T} . The estimated tension force vector expressed in the debris body-fixed frame is calculated using:

$$\underline{\hat{\boldsymbol{e}}} = \left(\underline{\boldsymbol{R}}_C + ({}^{\mathcal{O}}\boldsymbol{A}^{\mathcal{C}})^{\mathcal{C}}\underline{\boldsymbol{r}}_{t,C}\right) - \left(\underline{\boldsymbol{R}}_T + ({}^{\mathcal{O}}\hat{\boldsymbol{A}}^{T})^{\mathcal{T}}\underline{\boldsymbol{r}}_{t,T}\right)$$
(14a)

$$\underline{\hat{T}} = ({^{T}}\underline{\hat{A}}^{\mathcal{O}})(\tilde{T}\underline{\hat{e}}) \tag{14b}$$

where the rotation matrices $\mathcal{T}_{\mathbf{A}}^{\mathcal{O}}$ and $\mathcal{O}_{\mathbf{A}}^{\mathcal{T}}$ are created with the estimated attitude quaternion of the debris. For this work, it is assumed that the positions of the center of mass and the attachment points of the debris and chaser are known in their body-fixed frames.

The propagated quaternion representations $\underline{\hat{q}}_{k+1}(i)$ are then converted back to the original attitude error angle representations to recover the propagated $\underline{\chi}_{k+1}(i)$ points, through:

$$\underline{\hat{\mathbf{Sp}}}_{k+1}(0) = \underline{\mathbf{0}} \tag{15a}$$

$$\underline{\hat{\delta p}}_{k+1}(i) = \frac{\phi \hat{\underline{\delta \varrho}}_{k+1}(i)}{a + \hat{\delta q}_{4_{k+1}}(i)}$$
(15b)

where $\underline{\hat{\delta\varrho}}_{k+1}(i)$ and $\hat{\delta q}_{4_{k+1}}(i)$ are given by:

$$\underline{\hat{\delta q}}_{k+1}(i) = \left[\frac{\hat{\delta \varrho}_{k+1}(i)}{\hat{\delta q}_{4_{k+1}}(i)}\right] = \underline{\hat{q}}_{k+1}(i) \otimes \underline{\hat{q}}_{k+1}(0)$$
 (16)



predicted mean estimates can now be found using the restored $\underline{\underline{\chi}}_{k+1}(i) = [\underline{\delta p}_{k+1}^T(i), \underline{\hat{\underline{o}}}_{k+1}^T(i), \underline{\hat{\underline{J}}}_{k+1}^T(i)]^T$ points. The predicted state estimate and covariance are calculated by:

The Journal of the Astronautical Sciences

$$\hat{\underline{x}}_{k+1}^{-} = \sum_{i=0}^{2n} W_i^{\text{mean}} \underline{\chi}_{k+1}(i)$$
 (17a)

$$\mathbf{P}_{k+1}^{-} = \sum_{i=0}^{2n} W_i^{\text{cov}} [\underline{\mathbf{\chi}}_{k+1}(i) - \hat{\underline{\mathbf{x}}}_{k+1}^{-}] [\underline{\mathbf{\chi}}_{k+1}(i) - \hat{\underline{\mathbf{x}}}_{k+1}^{-}]^T + \mathbf{Q}$$
 (17b)

where the process noise covariance matrix is denoted with Q, and the weights for the *i*-th sigma point (i.e., W_i^{mean} and W_i^{cov}) are given by:

$$W_i^{\text{mean}} = \frac{\lambda}{n+\lambda}, \quad i = 0$$
 (18a)

$$W_i^{\text{cov}} = \frac{\lambda}{n+\lambda} + (1 - \alpha^2 + \beta), \quad i = 0$$
 (18b)

$$W_i^{\text{mean}} = W_i^{\text{cov}} = \frac{1}{2(n+\lambda)}, \quad i = 1, 2, ..., 2n$$
 (18c)

where the third tuning parameter β is used to incorporate prior knowledge of the distribution.

The mean estimates and covariance are then updated using pixel coordinate measurements of tracked features (i.e., $d_{x'}$ and $d_{y'}$) at discrete observation times, through a pinhole camera model (see Sect. 3). The mean predicted output \hat{y} is generated using the same model as \tilde{y} from Sect. 3, where the corresponding elements of \underline{v}_{k+1} consist of Gaussian random variables with a mean of 0 and covariance \mathbf{R}_{k+1} . To update the mean estimates, the mean predicted measurement $\underline{\Gamma}_{k+1}$ for each visible tracked feature is first found through:

$$\underline{\Gamma}_{k+1} = \sum_{i=0}^{2n} W_i^{\text{mean}} \underline{\gamma}_{k+1}(i)$$
 (19)

where $\gamma_{i+1}(i)$ is the predicted measurement of a tracked feature and is generated according to what is described in Eqs. (6)–(8) for each sigma point. Here, it should be noted that the expression for the position of a landmark in the camera frame uses the estimated quaternion from the filter to transform the position of the landmark from the debris body frame to the inertial frame in Eq. (8) (i.e., generation of $\gamma_{i+1}(i)$ uses ${}^{\mathcal{O}}\!\hat{A}^{T}$). Each $\underline{\Gamma}_{k+1}$ is then assembled to create the mean predicted measurement (i.e., $\hat{\underline{y}}_{k+1} = [\underline{\Gamma}_{k+1,1}^T, \dots, \underline{\Gamma}_{k+1,N_V}^T]^T$ for N_V visible tracked features). It should be noted that, while tension is measured by a sensor, the sensor output is not processed as a measurement and is used as a true tension value in the dynamics during the



prediction step. As such, the noise from the tension sensor is instead accounted for in the process noise matrix Q.

4.3 Prediction Update

Each $\underline{\chi}_{k+1}$ point is used in \underline{h} to generate the predicted pixel coordinate measurements from the camera model. The updated mean estimate and covariance can be calculated by:

$$\underline{\boldsymbol{\mu}}_{k+1} = \hat{\underline{\boldsymbol{x}}}_{k+1}^+ = \hat{\underline{\boldsymbol{x}}}_{k+1}^- + \boldsymbol{K}_{k+1}\underline{\boldsymbol{\varepsilon}}_{k+1} \tag{20a}$$

$$\mathbf{P}_{k+1}^{+} = \mathbf{P}_{k+1}^{-} - \mathbf{K}_{k+1} \mathbf{P}_{k+1}^{e_{y}e_{y}} \mathbf{K}_{k+1}^{T}$$
(20b)

where $\underline{\varepsilon}_{k+1}$ is the innovation, which is defined as:

$$\underline{\boldsymbol{\varepsilon}}_{k+1} = \underline{\tilde{\boldsymbol{y}}}_{k+1} - \underline{\hat{\boldsymbol{y}}}_{k+1}^{-} \tag{21}$$

To obtain the gain K_{k+1} and the innovation covariance $P_{k+1}^{e_y e_y}$, the output covariance P_{k+1}^{yy} and the cross-correlation matrix P_{k+1}^{xy} must first be found:

$$\mathbf{P}_{k+1}^{yy} = \sum_{i=0}^{2n} W_i^{\text{cov}} \left[\underline{\mathbf{\gamma}}_{k+1}(i) - \underline{\hat{\mathbf{y}}}_{k+1}^{-} \right] \left[\underline{\mathbf{\gamma}}_{k+1}(i) - \underline{\hat{\mathbf{y}}}_{k+1}^{-} \right]^T$$
(22a)

$$\boldsymbol{P}_{k+1}^{xy} = \sum_{i=0}^{2n} W_i^{\text{cov}} \left[\underline{\boldsymbol{\chi}}_{k+1}(i) - \hat{\underline{\boldsymbol{x}}}_{k+1}^{-} \right] \left[\underline{\boldsymbol{\gamma}}_{k+1}(i) - \hat{\underline{\boldsymbol{y}}}_{k+1}^{-} \right]^T$$
 (22b)

The innovation covariance is then computed as:

$$\mathbf{P}_{k+1}^{e_{y}e_{y}} = \mathbf{P}_{k+1}^{yy} + \mathbf{R}_{k+1} \tag{23}$$

and the gain is then obtained by:

$$\mathbf{K}_{k+1} = \mathbf{P}_{k+1}^{xy} (\mathbf{P}_{k+1}^{e_y e_y})^{-1}$$
 (24)

A thorough derivation of the UKF is provided by Crassidis and Markley et al. [45, 46]

5 Dynamics Simulation

5.1 Simulated System

Simulation of the dynamics of the tethered debris system is performed based on the chaser-tether-target simulation tool previously implemented by the authors [42], but with the addition of J2 perturbation, as described in Sect. 2. The simulator includes



the attitude dynamics of the chaser controlled by a sliding mode controller, and orbital dynamics of the system controlled by a Proportional-Integral-Derivative (PID) controller applied to the chaser spacecraft to maintain safety in the tug [29]. In particular, a sliding mode controller is employed on the chaser to ensure that its x-axis remains aligned with the tether. To maintain a desired tension in the tether, a PID controller is applied to a thruster pointing along the tether direction e on the chaser spacecraft to thrust directly away from the debris. The magnitude of the thrust force is determined by: $F(t) = \min(K_P e(t) + K_I \int_0^t e(\tau) d\tau + K_D \dot{e}(t), T_{max}),$ where the gains are selected to be $K_P = 300 \text{ kg/s}^2$, $K_L = 300 \text{ kg/s}^3$, and $K_D = 2000 \text{ kg/s}^3$ kg/s. The thrust on the chaser is therefore F(t)e. The error term is selected to be $e = \delta l + l_0 - l$, where δl is the desired elongation. Note that estimated values are not used in the control calculation, since estimation is performed during postprocessing; control performance is therefore unaffected by estimation performance in this work.

The Journal of the Astronautical Sciences

The parameters for the chaser, tether, and target for the simulations in this work are provided in Table 1, from which the spring constant of the tether can be found as $k = E\pi(d/2)^2/(l_0)$. The initial conditions for the simulations are presented in Table 2, where it can be noted that the initial chaser position remains to be determined. Three scenarios are generated using the provided initial conditions: The first scenario has an initial tether slackness of -1 m, and the second scenario has an initial tether elongation of 0.02 m (i.e., Scenario 1 is characterized by $(l - l_0) = -1$ m, and Scenario 2 is characterized by $(l - l_0) = 0.02$ m). Scenarios 1 and 2 have the same control saturation limits of $T_{max} = 2000$ N. In Scenario 3, the saturation limit is lowered to $T_{max} = 50$ N, and the initial slackness is $(l - l_0) = -0.2$ m. The initial position for the chaser in each scenario can be determined by $\underline{\mathbf{R}}_{C} = (\underline{\mathbf{R}}_{T} + {}^{\mathcal{I}}\underline{\mathbf{r}}_{t,T} + l^{\mathcal{I}}\underline{\mathbf{e}}) - {}^{\mathcal{I}}\underline{\mathbf{r}}_{t,C}.$

The UKF requires measurements of tension in the tether and pixel coordinates of the tracked landmarks on the target. Tension measurements are generated by injecting the tension history with noise. Pixel coordinate measurements are generated by converting the landmark positions into pixel coordinates via a pinhole

Table 1 Chaser, target, and tether parameters

Parameter	Value			
Chaser Inertia Matrix J_C (kg m ²)	diag(83.3, 83.3, 83.3)			
Target Inertia Matrix J_T (kg m ²)	diag(15000, 3000, 15000)			
Chaser Mass m_C (kg)	500			
Target Mass m_T (kg)	3000			
Tether Young's Modulus E (Pa)	60×10^9			
Tether Diameter d (m)	0.001			
Tether Natural Length l_0 (m)	30			
Tether Damping c (Ns/m)	16			
Tether Attachment Point, Chaser ${}^{C}\underline{r}_{t,C}$ (m)	$[0.5, 0, 0]^T$			
Tether Attachment Point, Target ${}^{\tau}\underline{\boldsymbol{r}}_{t,T}(\mathbf{m})$	$[0, -0.875, 0]^T$			



Table 2	Initial	conditions

Variable	Value
Target Position $\underline{\mathbf{R}}_T$ (km)	$[-6.176, -0.4208, 2.973]^T \times 10^3$
Chaser Velocity \underline{V}_C (km/s)	$[-2.45779, -4.40429, -5.71241]^T$
Target Velocity \underline{V}_T (km/s)	$[-2.45776, -4.40428, -5.71242]^T$
Chaser Attitude Quaternion q_{C} (-)	$[-0.5564, 0.6637, 0.4699, 0.1708]^T$
Target Attitude Quaternion q_T^{-C}	$[0.3214, -0.3830, 0.8138, 0.2962]^T$
Chaser Angular Velocity $\underline{\boldsymbol{\omega}}_{C}$ (rad/s)	$[0, 0, 0]^T$
Target Angular Velocity $\underline{\boldsymbol{\omega}}_{T}$ (rad/s)	$[0, 0.05, 0]^T$

projection model, then injecting noise into the pixel coordinates. The features being tracked are first selected as the tether attachment point on the target and between 1 and 4 additional features on the surface of the target to generate 4 differing sets per scenario. The sets include features at: (A) one corner (i.e., corner 1, L_{C1}) of the -y face of the target (i.e., debris face located at y = -0.875 m), (B) two corners of the target's -y face L_{C1} and L_{C2} , (C) two points on the sides of the debris in addition to Set (A) (i.e., feature L_{S1} on the face of the target at x = -0.625 m, feature L_{S2} on the face of the target at x = 0.625 m, and feature L_{C1} on a corner of the -y face of the debris body), and (D) two points on the sides of the debris in addition to Set (B) (i.e., L_{C1} , L_{C2} , L_{S1} , and L_{S2}). The positions of these features on the debris in the debris body-fixed frame are provided in Table 3. A visual representation of these positions on the debris is provided in Fig. 3. The normal vectors of the faces the tracked features are on are denoted by dashed arrows. The normal vector for the face that L_{C1} , L_{C2} , and L_t are attached to is $\underline{\boldsymbol{n}}_{L_{C1}} = \underline{\boldsymbol{n}}_{L_{C2}} = \underline{\boldsymbol{n}}_{L_t} = [0, -1, 0]^T$. The normal vectors for the faces L_{S1} and L_{S2} are attached to are $\underline{\boldsymbol{n}}_{L_{S1}} = [-1,0,0]^T$ and $\underline{\boldsymbol{n}}_{L_{\infty}} = [1,0,0]^T$, respectively. Here, all normal vectors are provided in the debris body-fixed frame.

5.2 Tension Effect on Target Motion and Measurement Generation

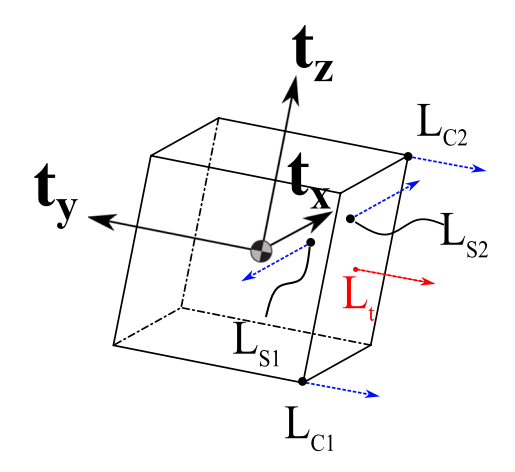
The tension measurements are generated by corrupting the true tension in the tether with noise that follows a Gaussian distribution with 0 mean and a standard deviation of 10 N, as based on the TE-RFS tension sensor [47]. If the measured tension is

Table 3 Tracked feature position on target debris in target body-fixed frame

Feature	x (m)	y (m)	z (m)
Attachment Point, \underline{r}_L	0	-0.8750	0
Corner 1, $\underline{r}_{L_{C1}}$	-0.6250	-0.8750	-0.6250
Corner 2, $\underline{r}_{L_{C2}}$	0.6250	-0.8750	0.6250
Side 1, $\underline{r}_{L_{S1}}$	-0.6250	-0.5833	0.4167
Side 2, $\underline{r}_{L_{S2}}$	0.6250	-0.5833	0.4167



Fig. 3 Position and normal vectors (dashed red and blue arrows) of the selected landmarks on the debris



negative (which could happen if, for example, the tension is smaller than 10 N), the measurement is considered to be 0 N. Figure 4 demonstrates an example of the noisy tension measurements obtained for each Scenario. The blue line is a history of generated tension measurement values and the black line is the true tension in the tether.

In Scenario 1, due to the large initial slackness of the tether, the tether undergoes a spike in tension early in the simulation, which then settles to around 15 N. Scenario 2 is characterized by a brief drop in tension from the initial value before also

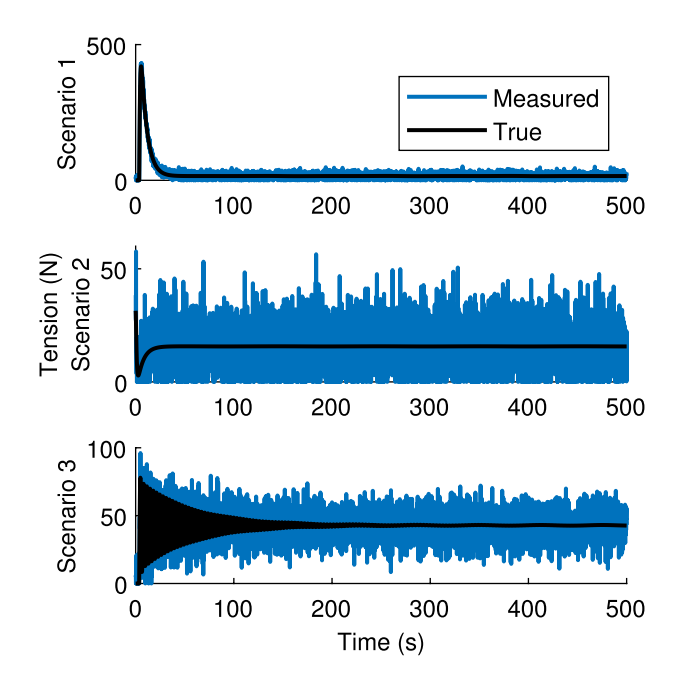


Fig. 4 True and measured tension magnitude for differing Scenarios



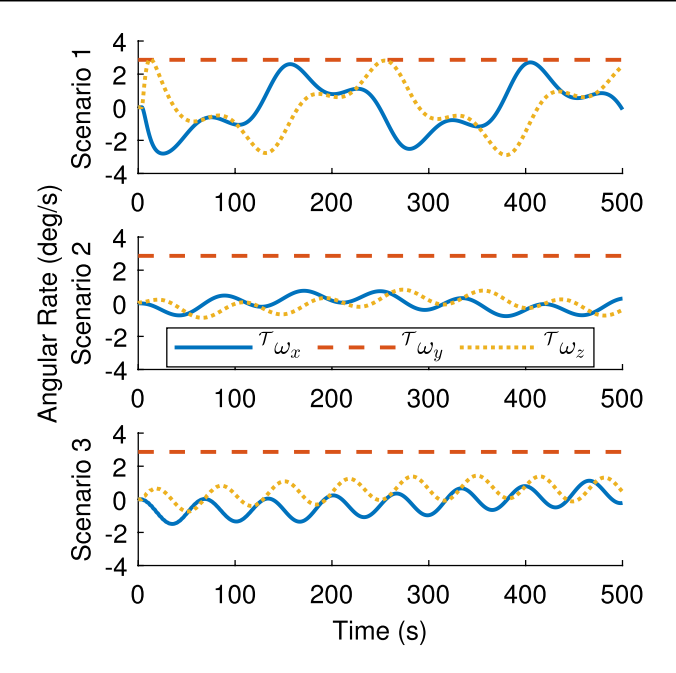


Fig. 5 Target angular rates for each Scenario

settling to around 15 N. Scenario 3 involves high-frequency oscillations of the true tether tension—at magnitudes significantly smaller than the initial spike in tension seen in Scenario 1—before settling to around 50 N. In each Scenario, it is clear that the noisy measurements can result in large deviations from the true value. For example, around 180 s of Senario 2 a tension measurement of approx. 56 N is returned for a true tension value of approx. 15 N, which is 273% higher than the true value. It should also be noted that, although the noise added to the tension measurement assumes a normal distribution, there are numerous occurrences of the measured tension being forced to 0 N in Scenarios 1 and 2. This action results in a skewed distribution of noise. During Scenario 3, these occurrences are limited to the first 20 s of simulation due to the true tension settling near 50 N instead of 15 N as with Scenarios 1 and 2.²

The effects on the angular velocity of the debris due to the tension profile caused by the initial conditions and the control of the chaser are displayed in Fig. 5. As the tether is attached directly to the y-axis of the debris, the tension is incapable of affecting ω_y of the debris in all Scenarios, and ω_y remains constant throughout the simulation. However, ω_x and ω_z are greatly affected by the tension profiles. Scenario 1 is characterized by larger ω_x and ω_z values of the debris, as compared to Scenarios 2 and 3. These large angular rates have the potential to make capture particularly

 $[\]overline{^2}$ This difference in final tension is due to a difference in control performance, where the control saturation during Scenario 3 prevents the tether from reaching the desired elongation.



dangerous. However, this Scenario is still studied in this work to investigate the effect large tensions and angular rates have on the estimation of the moments of inertia. Moreover, the large rotational rate makes it more difficult for tension in the tether to oppose debris rotation. The lower angular rates of Scenarios 2 and 3 result in safer capture of the debris. It should be noted that the angular rates for Scenarios 2 and 3 are similar, but a higher frequency in angular rate oscillation is present in Scenario 3. These lower angular rates enable the tether to better counteract the debris motion.

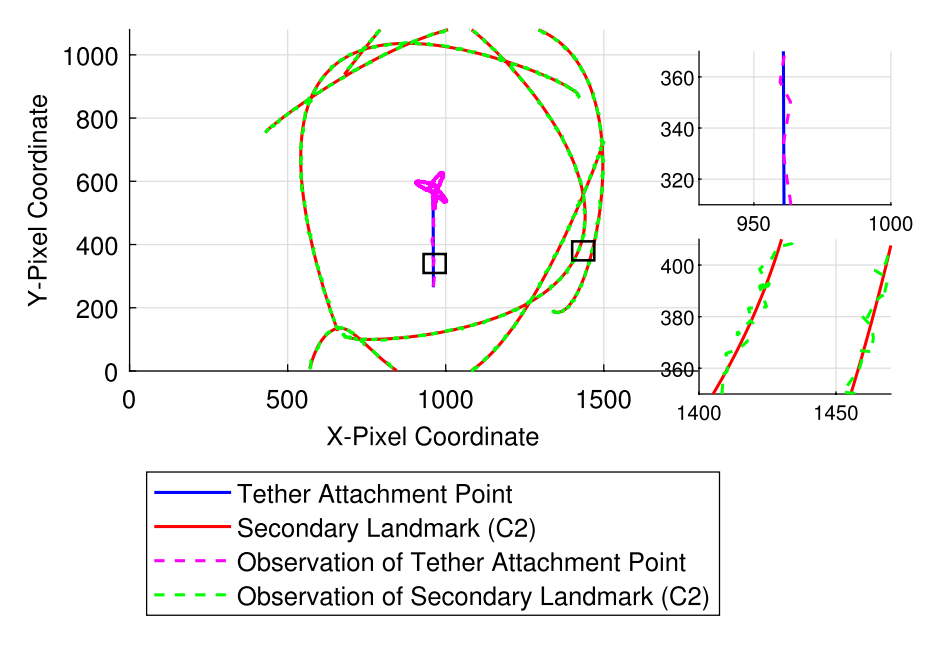
The Journal of the Astronautical Sciences

5.3 Camera Model Data Generation

As detailed in Sect. 3, the pixel-coordinate measurements of the landmarks are generated via a pinhole camera model that depends on the focal length, sensor size, sensor resolution, and principal point offset. A narrower FOV can be obtained either by using a longer focal length or a smaller sensor. The focal length is selected to be f = 200 mm and the sensor size is set to $20 \text{ mm} \times 11.25$ mm for this work. The resolution of the camera is 1920×1080 pixels, and the principal point offset is 0 such that the camera bore sight passes through the center of the image (i.e., c_x = 960 pixels and c_v = 540 pixels). The provided resolution and sensor size result in the image/world space scales to be calculated as $s_{x'} = 1920/20$ pixels/mm and $s_{\rm v'} = 1080/11.25$ pixels/mm. The noise follows a zero-mean Gaussian distribution with a standard deviation of 2 pixels. As with the tension measurements, pixel position measurements of the features are generated by adding noise to the true pixel position of the coordinate if it is within the FOV of the camera.

Examples of the pixel-coordinate time histories of L_t and of L_{C2} (both true and measured) for Scenarios 1 and 2 are presented in Fig. 6. The true and measured positions of the tether attachment point in the camera frame are shown with solid blue and dashed magenta lines, respectively. The true and measured positions of L_{C2} in time are shown in solid red and dashed green lines, respectively. Due to the small measurement error, the true and measured positions overlap closely; therefore, two zoomed sections are provided in each plot for the sake of clarity, where differences become apparent. It should be noted that there are multiple gaps in the position history of L_{C2} in Scenario 1 (see Fig. 6a). These gaps are caused either by L_{C2} leaving the FOV of the camera or being occluded by the debris body, and they represent periods when measurements would not be available for this secondary point. Unlike what happens in Scenario 1, L_{C2} is never occluded during Scenario 2, and visibility is only lost when L_{C2} exits the camera FOV (see Fig. 6b). The occlusion of L_{C2} in Scenario 1 demonstrates how the rapid rotation of the debris cannot be compensated for by the moment applied by the tension in the tether and therefore results in the additional loss of visibility of tracked features. In contrast to Scenario 1, Scenario 2 does not result in any occlusion and instead demonstrates how the tether may better counteract the debris rotation when the debris is rotating slowly. Although omitted in this work, the time history of L_{C2} in the camera frame during Scenario 3 is similar to Scenario 2.





a Scenario 1.

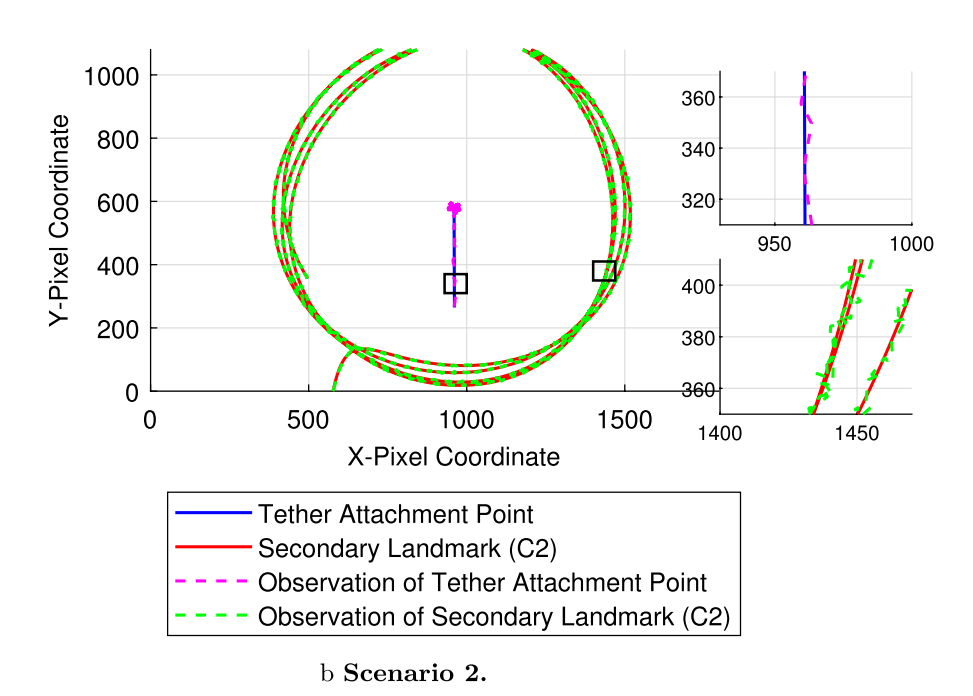


Fig. 6 True and measured pixel-coordinates of the tether attachment point and of Corner 2



5.4 Landmark Occlusion and Visibility

As exemplified by Fig. 6a, landmarks may be hidden from camera view due to the debris orientation. Points that are not visible due to being behind other parts of the object being observed are said to be "occluded." Occlusion is naturally captured when processing real-world images, or when rendering synthetic images (either by ray tracing or rasterization techniques). However, occlusion must be modeled separately here as detection of a feature on the target's surface is being simulated without image processing. For an arbitrary geometry, the occlusion of single points could be efficiently modeled by casting a ray from the camera to the point being tracked and checking if that ray intersects any of the defined geometry. As it is assumed that the target body is a cuboid geometry (a convex geometry), occlusion can be modeled using a much simpler technique whereby the direction of the vector n_t that is normal to the face with the landmark is checked as per:

$${}^{\mathcal{S}}\underline{\boldsymbol{n}}_{L} \cdot {}^{\mathcal{S}}\underline{\boldsymbol{S}}_{z'} > 0 \tag{25}$$

where $\underline{S}_{,,}$ is the z-direction of the camera frame as shown in Fig. 2. If the normal vector is pointed away from the camera, such that condition (25) is false, the landmark on that face is occluded and a measurement of it is not simulated (i.e., a measurement is not provided to the UKF for the occluded point). Conversely, if the normal vector of the feature is directed toward the camera (i.e., condition (25) is true), a measurement is simulated using the aforementioned camera projection model.

Plots showing the visibility of all the tracked features on the target during the simulation of each scenario are presented in Fig. 7. The blue-shaded region shows when the tether attachment point on the debris is visible to the camera. The visibility of L_{C1} is shown with the green shaded regions, whereas the visibility of L_{C2} is displayed with red shaded regions. The landmarks L_{S1} and L_{S2} are represented with black and magenta, respectively. While these plots correspond to the set where all 5 features are tracked in each Scenario, the visibility characteristics for a particular Set can be determined by ignoring the non-tracked features in each figure. As was observed in Scenarios 2 and 3 of Fig. 7, the debris experiences significantly less rotation than in Scenario 1; as a result, the features on the -y face (i.e., L_{C1} , L_{C2} , and L_t) are visible more often. It is noteworthy that Scenario 1 switches primarily between 1 and 4 visible points, with approx. 50% of the time spent with only 1 visible point. On the other hand, Scenarios 2 and 3 switch between 3 and 4 visible points frequently with a minimum of 3 points being visible for the vast majority of the simulation. In Scenarios 2 and 3, the temporary loss in the visibility of the landmarks on the -y face of the debris is due to the individual features leaving the FOV of the camera and not occlusion.

The percentage of the time each landmark is visible to the camera throughout the entire simulation for each Scenario is provided in Table 4. Note that each landmark is only visible for approx. 50% of the time during Scenario 1, further demonstrating how the rotation of the debris causes frequent loss of visibility for each landmark. Scenarios 2 and 3 have approx. the same average visibility time of a landmark at



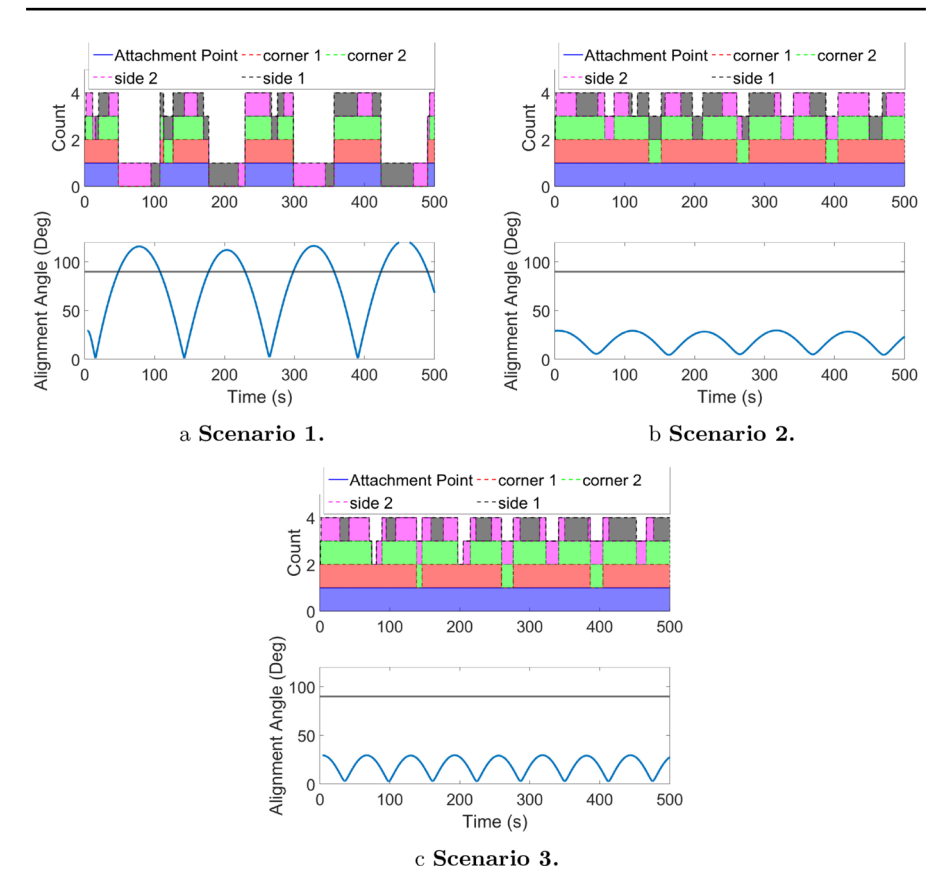


Fig. 7 Visibility of each tracked point during each Scenario

Table 4 Total simulation time percentage for landmark visibility

Landmark	Scenario 1	Scenario 2	Scenario 3
Tether Attachment Point, L_t	52.79%	100%	100%
Corner 1, L_{C1}	50.07%	89.54%	91.46%
Corner 2, L_{C2}	47.09%	86.80%	86.86%
Side 1, L_{S1}	50.37%	46.33%	38.27%
Side 2, L_{S2}	49.23%	51.77%	57.77%

75%, but the minimum visibility time for Scenario 2 is higher (see $L_{\rm S1}$) than for Scenario 3. In exchange for a lower minimum visibility time for a given feature, Scenario 3 has more visibility time for Corner 1, Corner 2, and Side 2. It is evident that Scenarios 2 and 3 have similar visibility patterns, therefore the major difference between these two Scenarios is the tension profile created by the PID controller and initial conditions.



The visibility of certain landmarks can be directly linked to the safety of the debris capture. The bottom half of each plot in Fig. 7 displays the alignment angle θ (defined in Fig. 1) of the tether with respect to the negative y-axis of the debris for each Scenario. When the alignment angle is greater than 90°, the tether begins to wrap around the debris, making rotation of the debris particularly unsafe. This is also linked to the occlusion of L_t , L_{C1} and of L_{C2} , as these features will be blocked by the debris body (see Fig. 7a). On the other hand, Scenarios 2 and 3 never experience an alignment angle larger than 90° (which is characteristic of safe rotational motion), and therefore have more landmarks visible overall. As the alignment angle does not surpass 90°, the periods in which a landmark on the -y face is lost in Scenarios 2 and 3 are due to the features leaving the FOV of the camera, and not due to the occlusion of the points (see Fig. 6). The alignment angle oscillations further prove that tension in the tether is better able to compensate for the rotational motion of the debris in Scenarios 2 and 3 than in Scenario 1. Therefore, from a safety perspective, it is clear that Scenarios 2 and 3 are preferred.

The Journal of the Astronautical Sciences

5.5 State Observability

To determine how observable the system is with the losses of tracked points, the observability Gramian is calculated [48]. First, the system dynamics must be linearized and the state transition matrix $\Phi_{k,k+1}$ must be computed. The linearized system is given as:

$$\underline{\dot{x}}(t) = A(\underline{x})\underline{x}(t) + B\underline{u}(t)
y(t) = C(x)x(t) + Du(t)$$
(26)

where A is the Jacobian of the state dynamics given in Eq. (13), and C is the Jacobian of the measurement model given in Eq. (6). The states x(t) are the attitude quaternion q, angular rates ω , and principal moments of inertia J_x , J_y , and J_z . The state transition matrix $\Phi_{k,k+1}$ from time step k to step k+1 may then be found via integration of $\Phi_k(t)$ over the time step where:

$$\Phi_{k,k+1} = \int_{t_k}^{t_{k+1}} \dot{\Phi}_k(t) dt$$

$$\dot{\Phi}_k(t) = A(\underline{x}(t))\Phi_k(t)$$

$$\Phi_k(t_k) = I_{10\times 10}$$
(27)

To properly calculate $\Phi_{k,k+1}$, the states \underline{x} must also be numerically integrated as in Eq. (13). The Gramian may then be calculated as:

$$\mathcal{G} = \sum_{k=1}^{o-1} \mathbf{\Phi}_{k,k+1}^T \mathbf{C}^T \mathbf{C} \mathbf{\Phi}_{k,k+1}$$
 (28)

where o is the total number of time steps. As the calculation of \mathcal{G} is too complex to do symbolically, \mathcal{G} is calculated numerically using the true states of the system at each time step. Due to the large disparity in available measurements between the attitude



and moment of inertia parameters of the debris (i.e., there are discrete measurements of pixel coordinates of tracked landmarks from which attitude is directly observable, but inertia parameters require multiple sequential measurements), the upper 7 rows of the Gramian matrix must be divided by 1×10^{10} to avoid scaling difficulties.

A plot of the rank of \mathcal{G} at each time-step for each Scenario is provided in Fig. 8. Each plot also displays the rank of the linear observability matrix assembled using the A and C matrices at each time step. It can be seen that the rank of the Gramian matrix rapidly grows to 10 (i.e., full rank) and remains full for the duration of the simulation. The longest period of time required for the Gramian matrix to achieve

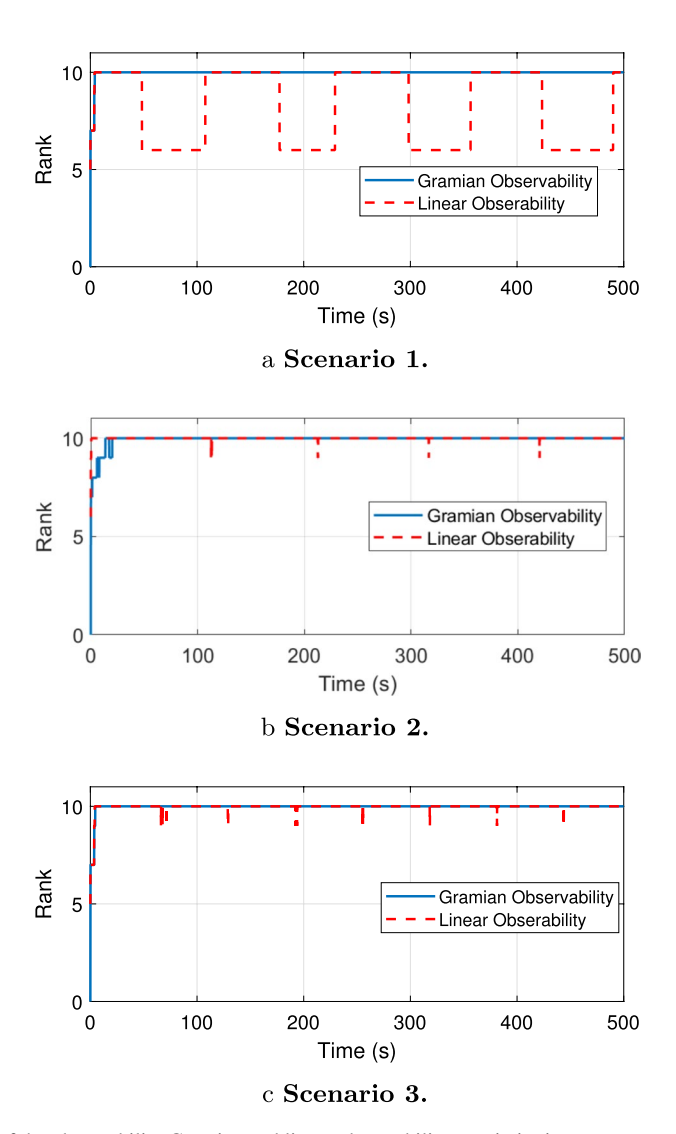


Fig. 8 Rank of the observability Gramian and linear observability matrix in time



full rank is found for Scenario 2, requiring approx. 18 s; this proves that every state can be estimated after 18 s. It should be noted that the linear observability matrices do not maintain full rank throughout the simulation, whereas the Gramian does. This is due to the fact that the linear observability matrix provides an instantaneous determination of observability, whereas the Gramian provides an overall observability throughout time. It should also be noted that, while the rank of ${\cal G}$ informs us of the observability of the system, at times where the rank is not full the observable or unobservable states may not be determined in this way.

6 Estimator Performance

In the following, the estimation performance is evaluated based on the distribution of the final moments of inertia estimates, the attitude estimates, and the angular velocity estimates throughout the simulations. It is assumed that the following quantities are known: (1) the position of the target and the chaser centers of mass, (2) the principal axes of the target, (3) the positions of the tether attachment point on the target and chaser in their respective body-fixed frames, (4) the positions of the landmarks in the target body-fixed frame, and (5) the chaser states and tether properties. Moreover, it should be noted that an image processing algorithm is not included in this work and it is assumed that matching of 3D features is available (e.g., with the Scale-Invariant Feature Transform algorithm [49]). Measurements are assumed to be received every 0.1 s and include the magnitude of tension in the tether, and pixel coordinates of the visible landmarks.³

Twelve simulations are run, comprised of 3 scenarios, each with 4 sets of tracked features. Recall that Scenario 1 is characterized by an initial tether slackness of 1 m, whereas Scenario 2 is characterized by an initial tether elongation of 2 cm, and Scenario 3 is characterized by an initial tether slackness of 0.2 m. Control saturation is 2000 N in Scenarios 1 and 2, and 50 N in Scenario 3. The tracked features on the debris are the tether attachment point L_t and combinations of additional landmarks creating the multiple Sets: (A) $\{L_{C1}\}$, (B) $\{L_{C1},L_{C2}\}$, (C) $\{L_{C1},L_{S1},L_{S2}\}$, (D) $\{L_{C1},L_{C2},L_{S1},L_{S2}\}$. The base scenario is selected to be Scenario 3 Set (D), where all the landmarks are tracked and the tether is initially slack with a low control saturation such that unreasonable control demand is avoided. This case is selected as the debris is safely captured (see Fig. 7) and tension in the tether is actively changing for a significant portion of the simulation as opposed to remaining constant for the majority of the simulation (see Fig. 4).

The filter is initialized with a variance matrix of $P = \text{diag}((1 \times 10^{-2} \text{ (rad)})^2, (1 \times 10^{-2} \text{ (rad)})^2, (1 \times 10^{-2} \text{ (rad/s)})^2, (1250 \text{ (kg m}^2))^2, (1250 \text{ (kg m}^2))^2)$. This matrix corresponds to the initial uncertainties in the three attitude error angles, three angular rates,

³ Recall that estimation is performed as a post-processing algorithm in this work. This explains the use of 10 Hz acquisition of images: a camera may take images rapidly and those images may be processed at a later time. Lower frequencies should be employed when accounting for image-processing algorithms.



and three principal moments of inertia. A Monte-Carlo simulation of 1000 runs is performed for each case, in which the initially estimated attitude quaternion for each of the 12 cases is the true attitude of the target debris. The initial attitude error angles are randomized with a Gaussian distribution with a mean of 0 and a standard deviation of 1×10^{-2} (rad). The initial distributions of the angular rates around their true values are also Gaussian with 0 mean and a standard deviation of 1×10^{-2} (rad/s). It is assumed that the initial moments of inertia distribution have a mean of 0 and a standard deviation of 1250 kg m² for J_x and J_z and 250 kg m² for J_y . The process noise is selected to be $Q = \text{diag}(1 \times 10^{-32} \text{ (rad/s)}, 1 \times 10^{-32} \text{ (rad/s)}, 1 \times 10^{-32})$ (rad/s), 3×10^{-9} (rad/s^2) , 3×10^{-9} (rad/s^2) , 3×10^{-9} (rad/s^2) , 0 $(kg m^2/s)$, 0 $(kg m^2/s)$ /s), 0 (kg m²/s)). The attitude dynamics of the debris are unaffected by disturbance sources and therefore have a small process noise. The process noise for the angular rate dynamics is larger than the attitude dynamics as the direct usage of tension measurements adds noise. The moments of inertia are assumed to be constant and therefore are not affected by process noise. The measurement covariance matrix is set to R = diag(4, 4, ..., 4), with the number of elements in the diagonal matching the number of visible tracked features at a particular timestep. The tunable parameters of the filter are selected to be $\alpha = 0.2$, $\beta = 1$, and $\kappa = -7$.

6.1 Performance of Estimation with Minor Debris Rotation and Varying Tension

Here, the performance of the estimator in the base scenario (Scenario 3, Set (D)) is investigated. Recall that a 50 N saturation limit is placed on the thrust control, causing a rapidly oscillating sinusoidal pattern in the tension profile during the simulation. The amplitude of oscillation is low enough that rapid debris rotation is not created; causing most landmarks to be visible for a significant portion of time. The only periods in which landmarks on the -y face of the debris are lost are when the landmarks exit the FOV of the camera (not due to occlusion). These conditions provide the most available information to the estimator for state estimation.

The time history of one randomly selected run of the Monte-Carlo simulation during Scenario 3 Set (D) is presented in Figs. 9 through 11. In each of these figures, the blue line shows the error between the estimated and true values, whereas the black line shows the $3-\sigma$ uncertainty bound of the error for the selected run. The Monte-Carlo statistics are shown as green, yellow, and red zones, with the green showing the $1-\sigma$ bound and red showing the $3-\sigma$ bound.

The error in the estimated attitude of the debris⁴ is shown in Fig. 9. During the majority of the simulation, the attitude error remains within 0.5° of the true attitude of the target, even during multiple periods of reduced certainty (e.g., around 75 s). These periods correspond to times in which features briefly exit the FOV of the camera (see Fig. 7). The largest uncertainties are found in the estimated p_x angle

⁴ It should be noted that these are not the attitude error angle states from the UKF. These values are calculated using the difference between the true and estimated attitude quaternions, then converted to p_x , p_y , and p_z angles for easier understanding.



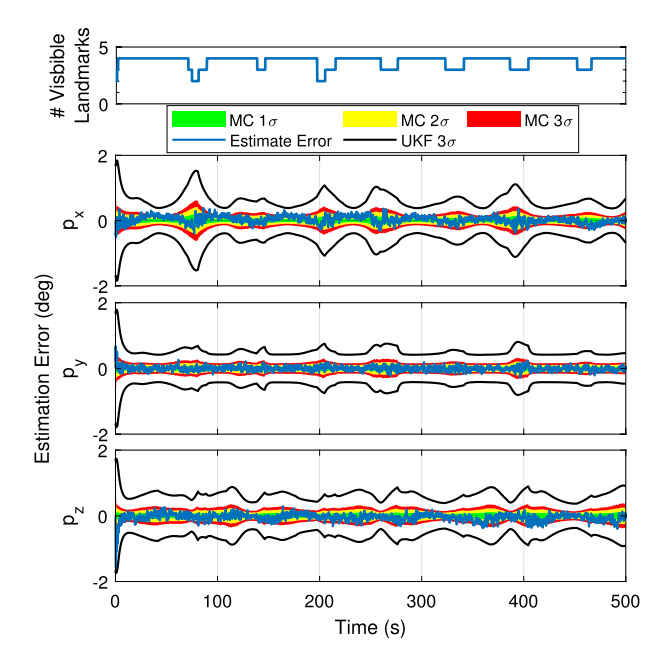


Fig. 9 Error in the estimated attitude of target debris

of the debris, where uncertainty reaches approx. 1.5° at times. However, even in this case, the Monte Carlo statistics show that the uncertainty should be approx. 0.6°

Figure 10 displays the error in the angular rate estimates throughout a single run of the UKF along with Monte Carlo statistics. Evidently, the filter is capable of estimating the angular rate well within 0.2 deg/s. Similarly to the attitude estimate results, the $3-\sigma$ bounds increase as the sight of landmarks is lost and

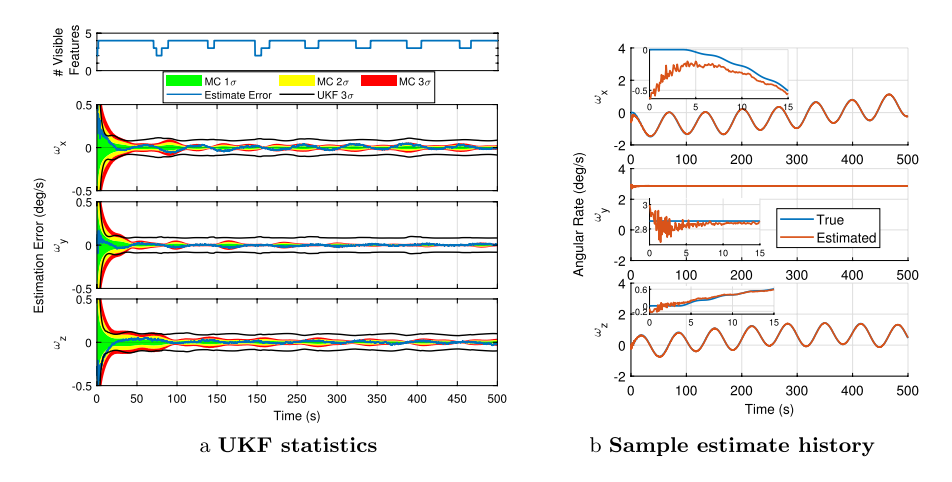


Fig. 10 Error in the estimated angular rates of target debris for Scenario 3 set (D)



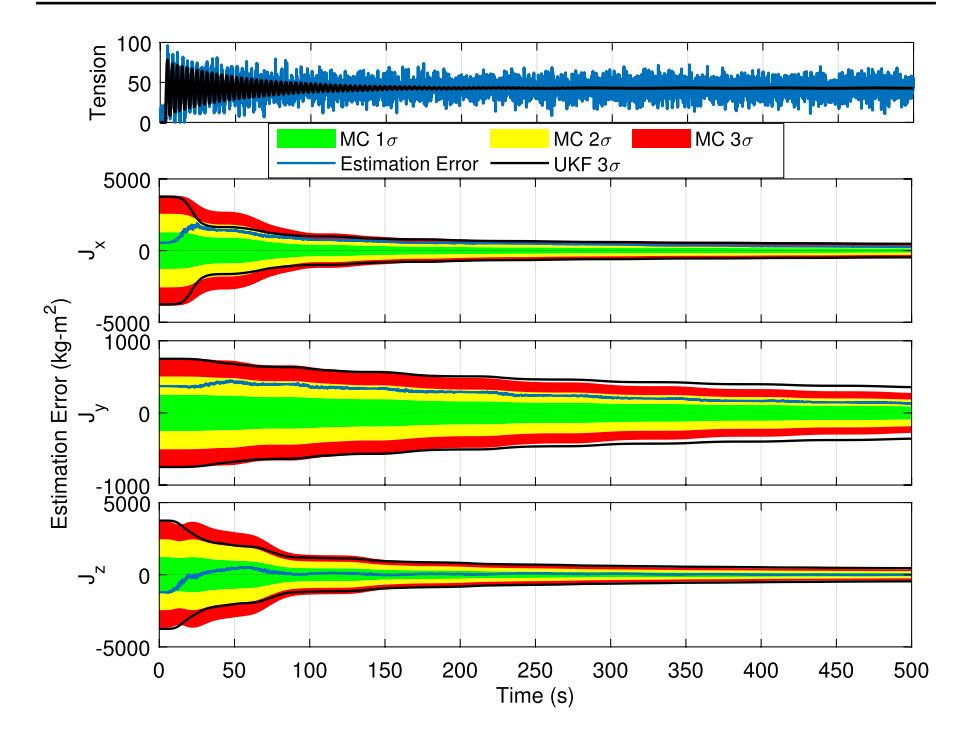


Fig. 11 Error in estimated target debris principal moments of inertia for Scenario 3 set (D)

decrease when landmarks re-enter the FOV of the camera. However, the worsening of the estimates is not significant when a landmark is lost. Additionally, notable is the fact that the filter has a smaller uncertainty than the Monte Carlo statistics during the first 50 s of simulation. After 50 s, the filter's uncertainty is again larger than the Monte Carlo distribution, but only by a small margin. A sample of the angular rate estimates and their true counterpart is provided in Fig. 10b, where it can be seen that the estimates are nearly identical to their respective true values. The greatest deviation between the estimate and the true value occurs at the initiation of the simulation; however, the angular rates quickly converge to their true values within 20 s.

The principal moments of inertia estimation results are presented in Fig. 11 in the same format as the attitude and angular rate results. One of the most notable differences in the estimator performance between the previous states and the moment of inertia estimates is the complete lack of increased uncertainty during periods in which a feature is lost, suggesting that the moment of inertia estimates are not directly affected by the visibility of tracked points on the target. It is also evident that uncertainty bounds returned by the filter closely match the Monte Carlo distribution throughout the majority of the simulation, with the uncertainty from the filter slightly larger than the Monte Carlo distribution. The uncertainties in J_x and J_z drastically decrease within 150 s and continue to slowly converge until the end of the simulation. The J_y bounds do not converge as significantly as



the J_x and J_z bounds during the initial 150 s of the simulation and instead experience a small convergence throughout the whole simulation.

The Journal of the Astronautical Sciences

The distributions of the errors in the final principal moment of inertia estimates across all 1000 runs are presented in Fig. 12. The errors are divided into bins of $50/30/50 \text{ kg m}^2$ for J_x , J_y , and J_z respectively, and the mean error and standard deviation of the errors are provided in the annotation. The solid black vertical lines denote the average final estimate errors, whereas the dashed lines display the $3-\sigma$ bounds of the final estimate errors for each MMI. Most impressive is the fact that the average estimate error for all 3 principal moments of inertia is below 100 kg m². When accounting for the standard deviation of the final J_x and J_z results, 99% of the final estimates fall within 3.59% and 2.95% of their true values, respectively. Although the absolute mean estimate error and standard deviation for J_y are both smaller in value than for J_x and J_z , 99% of the J_y estimates fall within 10.03% of its true value, which is a larger percent error (attributed to the fact that the true J_y value is 3000 kg m² as opposed to 15,000 kg m² for both J_x and J_z).

Overall for all states, the estimates improve in time from their initial values and almost always remain within the uncertainty bounds returned by the filter. The largest estimate errors outside of the uncertainty bounds returned by the filter can

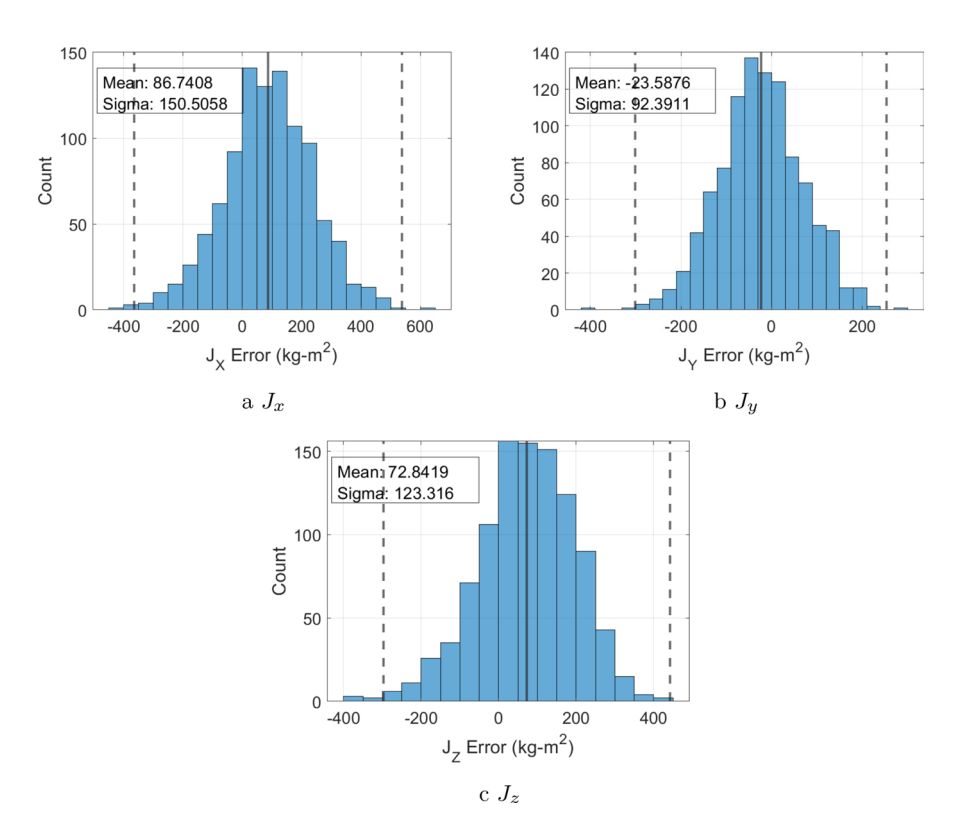


Fig. 12 Final principal moment of inertia estimate error distribution for Scenario 3 set (D)



be found in the $\underline{\omega}$, J_x , and J_z results, all of which occur prior to 100 s. The filter statistics closely match the Monte Carlo statistics when estimating the moments of inertia, but the filter undervalues its attitude and angular rate estimates for this Scenario and Set. Moreover, the final estimates of the principal moments of inertia are all accurate and precise after 500 s but can be considered to have been achieved earlier due to the slow convergence rate of the filter after the initial 150 s. It is also noted that, while the loss of tracked landmarks slightly affects the confidence in the attitude and angular rate estimates, there is almost no effect on the moments of inertia estimates.

6.2 Effect of Tracked Feature Visibility and Tension Profile on Estimator Statistics

While Scenarios 2 and 3 are characterized by multiple consistently visible tracked features, Scenario 1 suffers from long periods of lost landmark visibility and often only has a single visible feature. The loss of observed features directly affects the attitude and angular rate estimates of the filter, whereas the moments of inertia estimates are not as affected, as was already noticed by the consistent convergence of the principal moments of inertia in Scenario 3 Set (D) (see Fig. 11).

Figure 13 presents the attitude and angular rate estimation error together with the number of visible landmarks for Scenario 1 Set (D), in which the tether is initially slack by 1 m and rapid rotation causes unsafe dynamics and long periods of landmark occlusion. The rapid increase in filter uncertainty from occlusion of landmarks is most evident in the estimation of attitude (see Fig. 13a), which is characterized by large estimation errors and wide Monte Carlo distributions. When only one feature is visible, the attitude estimate quickly degrades with the worst error, of approx. 2°, occurring prior to 100 s. Once the tracked features reappear, shortly

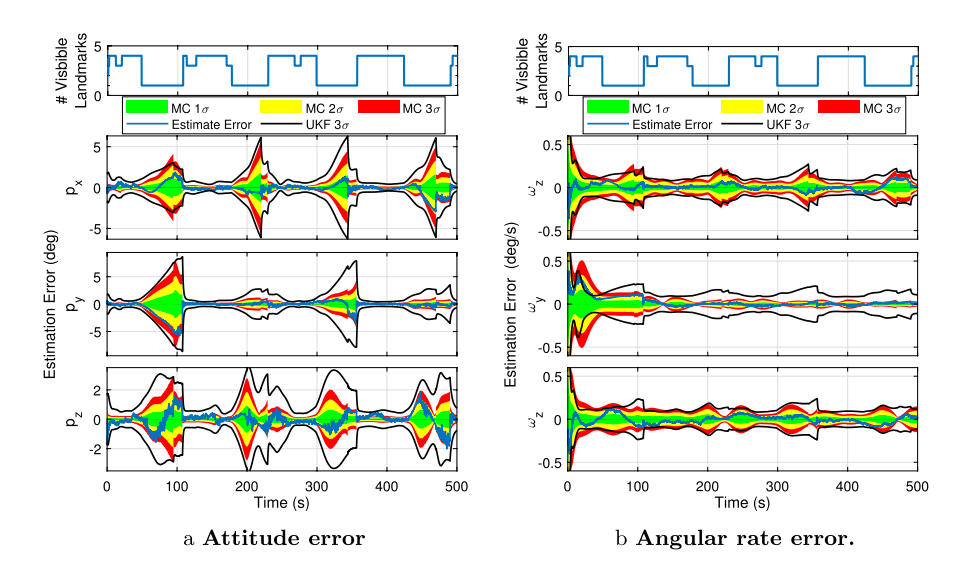


Fig. 13 Attitude and angular rate estimation errors for Scenario 1 Set (D)



after 100 s, a sharp improvement in uncertainty occurs, and attitude errors return to within 0.5°. Similar to the attitude estimates, the angular rate uncertainties (see Fig. 13b) also undergo periods of increased uncertainty when landmarks are lost. Although the increase in uncertainty is not as drastic as with the attitude estimates, sharp improvements are still evident when landmarks are reintroduced. Overall, it is clear that landmark visibility is very important for the quality of the attitude and angular rates of the debris.

The Journal of the Astronautical Sciences

While landmark visibility does not directly affect the moment of inertia estimates, the tension profile that leads to such visibility of the tracked points greatly affects the moment of inertia estimates. Tension profiles and MMI estimate errors for Scenarios 1 and 2 Set (D) are reported in Fig. 14. The reader may recall that Scenario 1 is characterized by a brief, large spike in tension (see Fig. 4), after which tension quickly reduces to 15 N within 50 s. In this time, the principal moments of inertia estimated by the filter rapidly converge, as can be seen in Fig. 14a. Similarly, in Scenario 2 set (D), the tension initially changes quickly and then settles to 15 N within 50 s (see Fig. 4). Again, it is observed in Fig. 14b that the majority of convergence for the moment of inertia estimates occurs around this brief period of changing tension. Going back to Fig. 11, it can be confirmed that convergence of the MMI estimate for Scenario 3 Set (D) also occurs primarily during the period of oscillatory tension in the tether, which continues until approx. 200 s; once tension has settled (in all Scenarios), the moment of inertia estimates remain roughly constant. From such results, it is clear that a varying tension is important for moment of inertia estimation and that the longer period of time in which tension in the tether changes, the more useful data will be available for estimation.

Comparing estimation results with landmark Set (D) in all scenarios, it is clear that Scenario 1 is not preferred for estimation; the rapid rotation of the debris

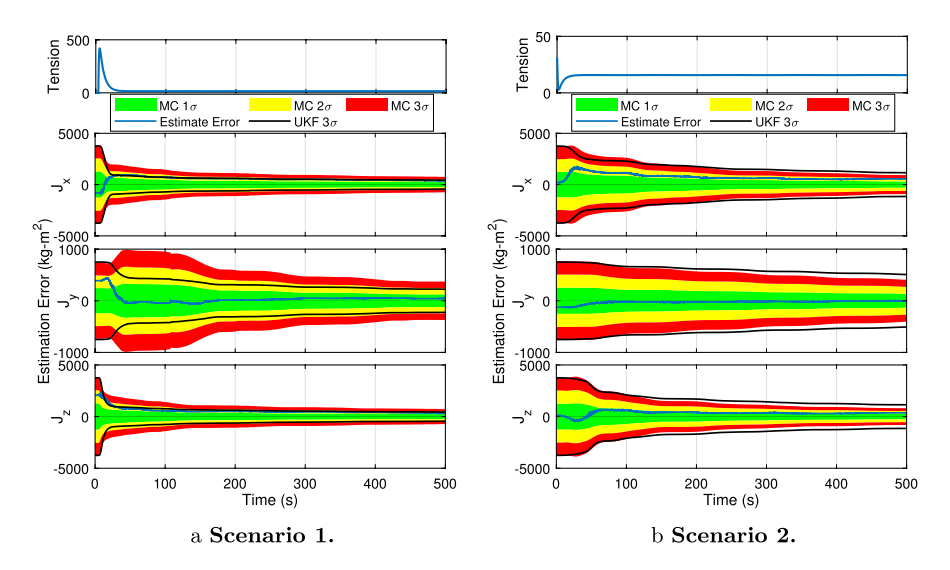


Fig. 14 Principal moment of inertia estimate error in time for Scenario 1 and Scenario 2 Set (D)



frequently causes loss of landmark visibility, which degrades the attitude and angular rate estimates returned by the filter and provides a short duration of useful data to estimate the mass moments of inertia. Debris motion in Scenario 2 allows the camera on the chaser to maintain a constant visual of most landmarks, however, Scenario 2 is still characterized by a short period of useful data for estimating the principal moments of inertia. It is evident that Scenario 3 provides the longest period of useful data for the UKF to estimate the moments of inertia while also maintaining accurate estimates for the attitude and angular rate of the debris, together with safe dynamics. Therefore, it can be concluded that for best estimation results, tension should vary for as long as possible without causing rapid rotation of the debris.

6.3 Effect of Chosen Tracked Features on Inertia Estimates

Although the filter is capable of accurately estimating the moments of inertia and states of the debris in all Scenarios with landmark Set (D), it is evident from the previous section that the number of visible points and the tension profile can greatly affect the performance of the estimator. In this Section, the performance of the filter at estimating the moments of inertia of the debris while tracking fewer than 5 landmarks for each Scenario is presented through Table 5, where data is organized from a higher to lower number of tracked landmarks. Here, the standard deviation σ_e and the means μ_e of the final estimated principal moments of inertia errors are provided as percentages of the true principal moments of inertia (i.e., STD = σ_e/J_{true} and Mean = μ_e/J_{true}). The sign before the mean error denotes whether the mean estimate is higher or lower than the true value, with the negative sign correlating to an estimate lower than the true value. To better visualize the data, the Table is color-coded. Color-coding of the mean error is based on the proximity of the average estimates to the true moment of inertia values: green shows means within 1% of the true value (i.e., 150 kg m² for J_z and J_x or 30 kg m² for J_y), yellow represents means between 1 and 4%, red shows means greater than 4% from the true value (i.e., 600 kg m² and 120 kg m² for J_x or J_z and J_y , respectively). The standard deviations are color-coded based on their values relative to the respective mean errors. The standard deviation

Table 5 Final estimated principal moment of inertia mean and standard deviation for each Set

Jx	Jv	_	l				Scenario 3		
	~ J	$_{ m Jz}$	Jx	$_{ m Jy}$	$_{ m Jz}$	Jx	Jy	$_{ m Jz}$	
2.00%	0.49%	1.84%	2.66%	0.39%	2.09%	0.58%	-0.79%	0.49%	
1.66%	4.10%	1.60%	2.06%	4.51%	1.81%	1.00%	3.08%	0.82%	
1.74%	-0.05%	1.60%	2.59%	0.29%	2.09%	0.52%	-0.91%	0.38%	
1.58%	3.94%	1.52%	2.18%	4.37%	1.90%	1.09%	3.34%	0.85%	
12.66%	13.96%	14.97%	2.70%	0.21%	2.15%	0.55%	-0.88%	0.50%	
21.39%	27.04%	26.21%	2.17%	4.41%	1.91%	1.03%	3.04%	0.90%	
6.18%	3.88%	6.70%	2.52%	0.19%	2.11%	0.46%	-1.21%	0.47%	
11.65%	13.29%	13.63%	2.20%	4.50%	1.96%	1.12%	3.68%	0.85%	
	1.66% 1.74% 1.58% 12.66% 21.39% 6.18%	1.66% 4.10% 1.74% -0.05% 1.58% 3.94% 12.66% 13.96% 21.39% 27.04% 6.18% 3.88%	1.66% 4.10% 1.60% 1.74% -0.05% 1.60% 1.58% 3.94% 1.52% 12.66% 13.96% 14.97% 21.39% 27.04% 26.21% 6.18% 3.88% 6.70%	1.66% 4.10% 1.60% 2.06% 1.74% -0.05% 1.60% 2.59% 1.58% 3.94% 1.52% 2.18% 12.66% 13.96% 14.97% 2.70% 21.39% 27.04% 26.21% 2.17% 6.18% 3.88% 6.70% 2.52%	1.66% 4.10% 1.60% 2.06% 4.51% 1.74% -0.05% 1.60% 2.59% 0.29% 1.58% 3.94% 1.52% 2.18% 4.37% 12.66% 13.96% 14.97% 2.70% 0.21% 21.39% 27.04% 26.21% 2.17% 4.41% 6.18% 3.88% 6.70% 2.52% 0.19%	$ \begin{array}{c ccccccccccccccccccccccccccccccccccc$	$\begin{array}{c ccccccccccccccccccccccccccccccccccc$	$\begin{array}{c ccccccccccccccccccccccccccccccccccc$	



is coded such that: $|\sigma_e - |\mu_e|| \le 0.5\%$ are green, $0.5\% < \sigma_e - |\mu_e| \le 4\%$ are yellow, and $\sigma_e - |\mu_e| < -0.5\%$ or $\sigma_e - |\mu_e| > 4\%$ are red. This scheme is selected as estimation of the MMI with minimal uncertainty (e.g., bound selected to be 0.5% of J_{true}) requires the true principal moment of inertia to be within $1-\sigma$ of the mean estimated value. If the standard deviation of the estimate errors is smaller than the mean error. then the true moment of inertia value lies outside of the 1- σ bound of the estimates: which represents estimation convergence to an incorrect moment of inertia value.

The Journal of the Astronautical Sciences

It is evident from Scenario 1 that the mean principal moments of inertia estimates from the filter are within 2% of the true value for Sets (C) and (D), where secondary landmarks are available on two sides of the debris. When tracking only landmarks on the -y face of the target (i.e., Sets (A) and (B)) however, the average estimate errors and corresponding standard deviations significantly increase, with worse estimates being apparent for Set (B). In Scenario 2, the filter is capable of estimating the moments of inertia with all Sets more reliably, within 3% for J_r and J_z and within 0.5% of the true J_y ; estimation under the conditions of Scenario 2 Sets (A) and (B) also demonstrates the filter's ability to estimate the mean (although with larger uncertainty than Scenario 3) with fewer tracked points on the target. Scenario 3 allows for the best estimator performance, with the closest average estimates to the true values with all Sets for J_r and J_z , and competitive average estimates for J_v : under most conditions, the filter can estimate all moments of inertia within 1% of their true values, with some slightly worse J_{ν} estimates for Sets (A) and (C). Despite a slightly larger error for the average J_{v} estimate than in Scenarios 1 and 2, the uncertainty in these estimates is lower.

To account for the possible mischaracterization of the uncertainty in an image processing algorithm, the performance of the estimator for various added measurement noise and estimator measurement noise matrix R combinations was also analyzed. Table 6 reports the results of this analysis for Scenario 3. In the first column is Case 1, which is the base case, where the measurement uncertainty and the added noise—ideally—match, with a noise variance of 4 pixels (i.e., $\sigma^2 = 4$ pixels² and $\mathbf{R} = \text{diag}(4, 4, ..., 4)$ pixels²); note that the results are the same as in Table 5. In the middle column is Case 2, where the filter uncertainty

Table 6 Estimation	on performance	with	mismatched	pixel	measurement	noise	and	uncertainty	for
Scenario 3									

Set\Case		Case 1				Case 2		Case 3		
		Jx	Jу	Jz	Jx	Jу	Jz	Jx	Jу	Jz
Set D	Mean	0.58%	-0.79%	0.49%	0.48%	-0.77%	0.17%	0.60%	-0.79%	0.44%
Set B	STD	1.00%	3.08%	0.82%	1.28%	3.81%	0.94%	1.04%	3.06%	0.83%
Set C	Mean	0.52%	-0.91%	0.38%	0.46%	-1.13%	0.12%	0.52%	-1.04%	0.42%
Det C	STD	1.09%	3.34%	0.85%	1.27%	3.92%	1.04%	1.08%	3.42%	0.91%
Set B	Mean	0.55%	-0.88%	0.50%	0.45%	-1.05%	0.25%	0.58%	-0.80%	0.48%
Set B	STD	1.03%	3.04%	0.90%	1.22%	4.04%	1.03%	1.03%	3.11%	0.89%
Set A	Mean	0.46%	-1.21%	0.47%	0.38%	-1.06%	0.19%	0.44%	-1.15%	0.50%
	STD	1.12%	3.68%	0.85%	1.33%	4.06%	0.99%	1.11%	3.49%	0.88%



 $(\mathbf{R} = \text{diag}(25, 25, ..., 25) \text{ pixels}^2)$ is greater than the variance of the noise in the pixel-coordinate measurements ($\sigma^2 = 4$ pixels²). The third column presents the Case 3 results, in which the filter has higher certainty in the measurements than the added noise variance (i.e., injected noise has $\sigma^2 = 25$ pixels² and the filter $\mathbf{R} = \text{diag}(4, 4, \dots, 4)$ pixels²). Notable is the fact that all changes in the final distribution of the estimated moments of inertia (for both the averages and standard deviations of the final estimates) are less than 1% for Case 2 and less than 0.2% for Case 3. It is evident that the average estimates are not significantly degraded by mismatched noise parameters, with Case 2 having slightly larger errors in the average J_{ν} estimates. Mismatched uncertainty has a larger effect on the distribution of the final estimates of the filter, in which Case 2 is again most affected by greater uncertainty. The most notable effects of mismatched R values from the true noise values is the decreased ability of the UKF to estimate the principal moments of inertia with minimal uncertainty in Case 2, and a minor change in this ability for Case 3. Overall, while mismatched measurement uncertainty will affect the Kalman filter final estimate performance, the effects of an incorrectly characterized image processing algorithm in either direction (i.e., values in the R matrix higher or lower than the actual noise from the image-processing algorithm) appear not to degrade performance significantly.

Although, as demonstrated in the previous section, the visibility of landmarks does not directly affect the moment of inertia estimates, it is clear that the chosen tracked points and the motion caused by different tension profiles (driven by initial conditions and the controller) greatly affect the quality of estimation. Due to the rapid rotation of the debris, caused by the moment applied by the spike in tension in Scenario 1, the camera loses visibility of landmarks for significant portions of the simulation and results in significant degradation of the final accuracy and precision of the moment of inertia estimates. When not affected by large tension, the debris rotates at a slower rate, which results in longer periods of visibility for all landmarks. This increased observation time allows the estimator to require fewer observable points to obtain the principal moments of inertia accurately. Longer periods of changing tension (such as in Scenario 3) result in an average estimate closer to the true moments of inertia. Overall, it could be concluded that lower tension magnitudes with longer periods of changing tension are preferable over short, large bursts of tension, for effective estimation of debris parameters. This is especially evident as fewer available landmarks are sufficient to accurately and precisely estimate the principal moments of inertia.

7 Conclusion

This work enhances prior estimation work through the simulation of occlusion, the inclusion of J2 perturbation in the system dynamics, an observability analysis, the investigation of desired conditions for estimation, and an analysis of necessary landmark tracking. The dynamics and control of tether-captured debris were simulated, with PID control applied to thrusters on the chaser to maintain



a desired tension in the tether. Three Scenarios were investigated in which, (1) the tether is initially slack with a high controller saturation limit, (2) the tether is initially taut with a high controller saturation limit, and (3) the tether is initially slack with a low saturation limit.

The Journal of the Astronautical Sciences

It was assumed that pixel-coordinate measurements of 2 to 5 tracked features and the tension magnitude in the tether are frequently made available to a UKF by sensors. It was further assumed that the orbital positions of the chaser and target, and the position of the landmarks on the target body in the target body frame are known. Finally, it was assumed that the principal axes of the target are known. With such assumptions and with the estimation of the target attitude, the estimated tension vector may be calculated, allowing estimation of the moment affecting the target, and therefore estimation of the principal moments of inertia of the target.

To ensure estimation is possible within the assumptions, the observability Gramian was analyzed. It was confirmed that the observability Gramian matrix is full rank and therefore all states estimated in the filter are observable. Although all states are observable, it was found that the performance of the UKF is heavily affected by the number of tracked landmarks and the tension profile of the tether. Less tracked features result in poor estimation if there is a brief period of large tension that causes rapid rotation of the debris and occlusion of landmarks. However, a longer period of changing tension with a small magnitude allows the UKF to accurately estimate the moments of inertia even with very few landmarks. When landmarks are occluded due to rapid debris motion caused by the tension, the precision of the attitude and angular rate estimates often drops, whereas angular rate accuracy often remains high. Loss of visibility of tracked landmarks does not worsen moment of inertia estimates, but does affect final estimate accuracy and precision. On average, the filter is capable of estimating the moments of inertia both accurately and precisely when tracking at least 4 landmarks. It was also found that no significant degradation in estimation results occurs if the measurement covariance matrix and the noise covariance have mismatched characteristics.

Overall, it was shown that the UKF is capable of estimating the attitude and angular rates of the debris precisely and accurately given enough landmarks with any control profile. However, from the results of this work, it can be concluded that it is best to avoid control profiles that result in large tensions and rapid rotation of the debris. In fact, not only is the debris motion unsafe, but there is also no benefit to estimation. Preferred profiles will include low tension magnitudes that allow for slow rotation of the debris while maintaining long periods of changing tension.

In the future, the authors plan on relaxing the assumptions made for this work, such as the perfect knowledge of the positions of the tether attachment point and of the tracked landmarks in the target body frame. Moreover, the estimation algorithm will be implemented in series with the control algorithm, such that estimation results will both affect and be affected by the control algorithm. In doing so, the measurement frequencies will need to better reflect on-line performance of the sensors and related algorithms.



Acknowledgements This work was funded by the National Science Foundation (NSF), under the CMMI Program, Award number 2105011. Derek Bourabah also acknowledges reception of the NASA Space Grant Fellowship. Chris Gnam also acknowledges reception of the National Science Foundation's Graduate Research Fellowship, which helped to support his contribution to this work under Grant No. 2020305048. The authors would like to acknowledge Dr. John Crassidis for helpful discussions.

Data availability All data generation techniques during this study are included in this published article. The code created for the current study is available from the corresponding author upon request.

Declarations

Conflict of interest The authors declare that they have no conflict of interest.

References

- Pardini, C., Anselmo, L.: Review of past on-orbit collisions among cataloged objects and examination of the catastrophic fragmentation concept. Acta Astronaut. 100, 30–39 (2014). https://doi.org/ 10.1016/j.actaastro.2014.03.013
- 2. Miller, R. (ed.): Orbital Debris Quarterly News 25(4) (2021)
- Liou, J.C., Johnson, N.L., Hill, N.M.: Controlling the growth of future LEO debris populations with active debris removal. Acta Astronaut. 66(5–6), 648–653 (2010). https://doi.org/10.1016/j.actaastro. 2009.08.005
- Castronuovo, M.M.: Active space debris removal—A preliminary mission analysis and design. Acta Astronaut. 69(9–10), 848–859 (2011). https://doi.org/10.1016/j.actaastro.2011.04.017
- Liou, J.C.: An active debris removal parametric study for LEO environment remediation. Adv. Space Res. 47(11), 1865–1876 (2011). https://doi.org/10.1016/j.asr.2011.02.003
- Virgili, B., Krag, H.: Analyzing the criteria for a stable environment. In: 2011 AAS/ AIAA Astrodynamics Specialist Conference, vol. 142 (Girdwood, Alaska, 2011). AAS 11–411
- Bischof, B.: ROGER-Robotic geostationary orbit restorer. In: 54th International Astronautical Congress of the International Astronautical Federation, the International Academy of Astronautics, and the International Institute of Space Law (Bremen, Germany, 2003). IAA–5
- 8. Wormnes, K., de Jong, J.H., Krag, H., Visentin, G.: Throw-nets and tethers for robust space debris capture. In: Proceedings of the 64th International Astronautical Congress (Beijing, China, 2013). IAC-13, A6.5, 2x16445
- Lavagna, M., Pesce, V., Bevilacqua, R.: Uncooperative objects pose, motion and inertia tensor estimation via stereovision. In: Advanced Space Technologies for Robotics and Automation 2015. Noordwijk, Netherlands (2015)
- Botta, E.M., Miles, C., Sharf, I.: Simulation and tension control of a tether-actuated closing mechanism for net-based capture of space debris. Acta Astronaut. 174, 347–358 (2020). https://doi.org/10.1016/j.actaastro.2020.04.052
- Huang, W., He, D., Li, Y., Zhang, D., Zou, H., Liu, H., Yang, W., Qin, L., Fei, Q.: Nonlinear dynamic modeling of a tether-net system for space debris capture. Nonlinear Dyn. 110(3), 2297– 2315 (2022). https://doi.org/10.1007/s11071-022-07718-7
- Aslanov, V.S., Yudintsev, V.V.: Behavior of tethered debris with flexible appendages. Acta Astronaut. 104(1), 91–98 (2014). https://doi.org/10.1016/j.actaastro.2014.07.028
- 13. Dudziak, R., Tuttle, S., Barraclough, S.: Harpoon technology development for the active removal of space debris. Adv. Space Res. 56(3), 509–527 (2015). https://doi.org/10.1016/j.asr.2015.04.012
- Aglietti, G.S., Taylor, B., Fellowes, S., Ainley, S., Tye, D., Cox, C., Zarkesh, A., Mafficini, A., Vinkoff, N., Bashford, K., Salmon, T., Retat, I., Burgess, C., Hall, A., Chabot, T., Kanani, K., Pisseloup, A., Bernal, C., Chaumette, F., Pollini, A., Steyn, W.H.: RemoveDEBRIS: an in-orbit demonstration of technologies for the removal of space debris. Aeronaut. J. 124(1271), 1–23 (2019). https://doi.org/10.1017/aer.2019.136
- Huang, P., Wang, D., Meng, Z., Liu, Z.: Post-capture attitude control for a tethered space robottarget combination system. Robotica 33(4), 898–919 (2014). https://doi.org/10.1017/s026357471 4000617



16. Huang, P., Wang, D., Meng, Z., Zhang, F., Guo, J.: Adaptive postcapture backstepping control for tumbling tethered space robot-target combination. J. Guid. Control. Dyn. 39(1), 150-156 (2016). https://doi.org/10.2514/1.G001309

The Journal of the Astronautical Sciences

- 17. Zhao, Y., Huang, P., Zhang, F.: Dynamic modeling and super-twisting sliding mode control for tethered space robot. Acta Astronaut. 143, 310–321 (2018), https://doi.org/10.1016/j.actaastro.2017.11.
- 18. Huang, P., Zhang, F., Chen, L., Meng, Z., Zhang, Y., Liu, Z., Hu, Y.: A review of space tether in new applications. Nonlinear Dyn. 94(1), 1–19 (2018). https://doi.org/10.1007/s11071-018-4389-5
- 19. Jasper, L., Schaub, H.: Input shaped large thrust maneuver with a tethered debris object. Acta Astronaut. 96, 128-137 (2014). https://doi.org/10.1016/j.actaastro.2013.11.005
- 20. Aslanov, V.S.: Chaos behavior of space debris during tethered tow. J. Guid. Control. Dyn. 39(10), 2399-2405 (2016). https://doi.org/10.2514/1.G001460
- 21. Aslanov, V.S., Yudintsev, V.V.: Chaos in tethered tug-debris system induced by attitude oscillations of debris. J. Guid. Control. Dyn. 42(7), 1630-1637 (2019). https://doi.org/10.2514/1.G004162
- Yu, B.S., Xu, S.D., Jin, D.P.: Chaos in a tethered satellite system induced by atmospheric drag and earth's oblateness. Nonlinear Dyn. 101(2), 1233-1244 (2020). https://doi.org/10.1007/ s11071-020-05844-8
- 23. Qi, R., Misra, A.K., Zuo, Z.: Active debris removal using double-tethered space-tug system. J. Guid. Control. Dyn. 40(3), 722–730 (2017). https://doi.org/10.2514/1.G000699
- 24. Yudintsey, V., Aslanov, V.: Detumbling space debris using modified yo-yo mechanism. J. Guid. Control. Dyn. 40(3), 714-721 (2017). https://doi.org/10.2514/1.G000686
- 25. Wang, B., Meng, Z., Huang, P.: Attitude control of towed space debris using only tether. Acta Astronaut. 138, 152–167 (2017). https://doi.org/10.1016/j.actaastro.2017.05.012
- 26. O'Connor, W.J., Hayden, D.J.: Detumbling of space debris by a net and elastic tether. J. Guid. Control. Dyn. 40(7), 1832-1836 (2017). https://doi.org/10.2514/1.G001838
- 27. Kang, J., Zhu, Z.H.: Dynamics and control of de-spinning giant asteroids by small tethered spacecraft. Aerosp. Sci. Technol. (2019). https://doi.org/10.1016/j.ast.2019.105394
- Zhang, Z., Yu, Z., Zhang, Q., Zeng, M., Li, S.: Dynamics and control of a tethered space-tug system using Takagi-Sugeno fuzzy methods. Aerosp. Sci. Technol. 87, 289-299 (2019). https://doi.org/10. 1016/j.ast.2019.02.033
- Field, L., Botta, E.M.: Relative distance control of uncooperative tethered debris. J. Astronaut. Sci. 70, 6 (2023). https://doi.org/10.1007/s40295-023-00422-7
- 30. Murotsu, Y., Senda, K., Ozaki, M., Tsujio, S.: Parameter identification of unknown object handled by free-flying space robot. J. Guid. Control. Dyn. 17(3), 488–494 (1994). https://doi.org/10.2514/3.
- 31. Ma, O., Dang, H., Pham, K.: On-orbit identification of inertia properties of spacecraft using a robotic arm. J. Guid. Control. Dyn. 31(6), 1761-1771 (2008). https://doi.org/10.2514/1.35188
- Nguyen-Huynh, T.C., Sharf, I.: Adaptive reactionless motion and parameter identification in postcapture of space debris. J. Guid. Control. Dyn. 36(2), 404-414 (2013). https://doi.org/10.2514/1. 57856
- 33. Zhang, T., Yue, X., Ning, X., Yuan, J.: Stabilization and parameter identification of tumbling space debris with bounded torque in postcapture. Acta Astronaut. 123, 301–309 (2016). https://doi.org/10. 1016/j.actaastro.2016.04.007
- 34. Peng, J., Xu, W., Pan, E., Yan, L., Liang, B., Wu, A.: Dual-arm coordinated capturing of an unknown tumbling target based on efficient parameters estimation. Acta Astronaut. 162, 589-607 (2019). https://doi.org/10.1016/j.actaastro.2019.03.008
- 35. Chu, Z., Ma, Y., Hou, Y., Wang, F.: Inertial parameter identification using contact force information for an unknown object captured by a space manipulator. Acta Astronaut. 131, 69-82 (2017). https:// doi.org/10.1016/j.actaastro.2016.11.019
- Tweddle, B.E.: Computer vision-based localization and mapping of an unknown, uncooperative and spinning target for spacecraft proximity operations. Ph.D. thesis, Massachusetts Institute of Technology (2013)
- 37. Tweddle, B.E., Saenz-Otero, A., Leonard, J.J., Miller, D.W.: Factor graph modeling of rigid-body dynamics for localization, mapping, and parameter estimation of a spinning object in space. J. Field Robot. 32(6), 897–933 (2015). https://doi.org/10.1002/rob.21548
- 38. Corpino, S., Mauro, S., Pastorelli, S., Stesina, F., Biondi, G., Franchi, L., Mohtar, T.: Control of a noncooperative approach maneuver based on debris dynamics feedback. J. Guid. Control. Dyn. 41(2), 431–448 (2018). https://doi.org/10.2514/1.G002685



- Lichter, M.D., Dubowsky, S.: State, shape, and parameter estimation of space objects from range images. In: IEEE International Conference on Robotics and Automation, vol. 3 (IEEE), pp. 2974– 2979. https://doi.org/10.1109/ROBOT.2004.1307513
- 40. Meng, Q., Liang, J., Ma, O.: Identification of all the inertial parameters of a non-cooperative object in orbit. Aerosp. Sci. Technol. 91, 571–582 (2019). https://doi.org/10.1016/j.ast.2019.05.047
- Zhang, F., Sharf, I., Misra, A., Huang, P.: On-line estimation of inertia parameters of space debris for its tether-assisted removal. Acta Astronaut. 107, 150–162 (2015). https://doi.org/10.1016/j.actaa stro.2014.11.016
- Bourabah, D., Field, L., Botta, E.M.: Estimation of uncooperative space debris inertial parameters after tether capture. Acta Astronaut. 202, 909–926 (2023). https://doi.org/10.1016/j.actaastro.2022. 07.041
- 43. Bourabah, D., Gnam, C., Botta, E.M.: Inertia tensor estimation of tethered debris through tether tracking. Acta Astronaut. 212, 643–653 (2023). https://doi.org/10.1016/j.actaastro.2023.08.021
- Vallado, D.A.: Fundamentals of Astrodynamics and Applications, 5th edn. Microcosm Press, Cleveland (2022)
- Crassidis, J.L., Markley, F.L.: Unscented filtering for spacecraft attitude estimation. J. Guid. Control. Dyn. 26(4), 536–542 (2003). https://doi.org/10.2514/2.5102
- Crassidis, J.L., Markley, F.L., Cheng, Y.: Survey of nonlinear attitude estimation methods. J. Guid. Control. Dyn. 30(1), 12–28 (2007). https://doi.org/10.2514/1.22452
- TE-RFS multi-configuration tension sensor. https://www.checkline.com/tension_sensors/te-rfs. Accessed 25 Jan 2024
- Krener, A.J., Ide, K.: Measures of unobservability. In: Proceedings of the 48h IEEE Conference on Decision and Control (CDC) held jointly with 2009 28th Chinese Control Conference (2009), pp. 6401–6406. https://doi.org/10.1109/CDC.2009.5400067
- Lowe, D.G.: Distinctive image features from scale-invariant keypoints. Int. J. Comput. Vision 60(2), 91–110 (2004). https://doi.org/10.1023/b:Visi.0000029664.99615.94

Publisher's Note Springer Nature remains neutral with regard to jurisdictional claims in published maps and institutional affiliations.

Springer Nature or its licensor (e.g. a society or other partner) holds exclusive rights to this article under a publishing agreement with the author(s) or other rightsholder(s); author self-archiving of the accepted manuscript version of this article is solely governed by the terms of such publishing agreement and applicable law.

